

# Multi-dimensional Features of Neutrino Transfer in Core-Collapse Supernovae

K. Sumiyoshi

Numazu College of Technology, Ooka 3600, Numazu, Shizuoka 410-8501, Japan

sumi@numazu-ct.ac.jp

T. Takiwaki<sup>1</sup>

National Astronomical Observatory of Japan, 2-21-1 Osawa, Mitaka, Tokyo 181-8588,  
Japan

takiwaki.tomoya@nao.ac.jp

H. Matsufuru

Computing Research Center, High Energy Accelerator Research Organization 1-1 Oho,  
Tsukuba, Ibaraki 305-0801, Japan

hideo.matsufuru@kek.jp

and

S. Yamada

Science and Engineering & Advanced Research Institute for Science and Engineering,  
Waseda University, Okubo, 3-4-1, Shinjuku, Tokyo 169-8555, Japan

shoichi@heap.phys.waseda.ac.jp

Received \_\_\_\_\_; accepted \_\_\_\_\_

Revised version accepted for publication in *Astrophys. J.*

## ABSTRACT

We study the multi-dimensional properties of neutrino transfer inside supernova cores by solving the Boltzmann equations for neutrino distribution functions in genuinely six dimensional (6D) phase space. Adopting representative snapshots of the post-bounce core from other supernova simulations in three dimensions, we solve the temporal evolutions to stationary states of neutrino distribution functions by our Boltzmann solver. Taking advantage of the multi-angle and multi-energy feature realized by the  $S_n$  method in our code, we reveal the genuine characteristics of spatially three dimensional (3D) neutrino transfer such as non-radial fluxes and non-diagonal Eddington tensors. In addition, we assess the ray-by-ray approximation, turning off the lateral-transport terms in our code. We demonstrate that the ray-by-ray approximation tends to propagate fluctuations in thermodynamical states around the neutrino-sphere along each radial ray and overestimate the variations between the neutrino distributions on different radial rays. We find that the difference in the densities and fluxes of neutrinos between the ray-by-ray approximation and the full Boltzmann transport becomes  $\sim 20\%$ , which is also the case for the local heating rate, whereas the volume-integrated heating rate in the Boltzmann transport is found to be only slightly larger ( $\sim 2\%$ ) than the counterpart in the ray-by-ray approximation due to cancellation among different rays. These results suggest that we had better assess carefully the possible influences of various approximations in the neutrino transfer employed in the current simulations on supernova dynamics. Detailed information on the angle and energy moments of neutrino distribution functions will be profitable for the future development of numerical methods in neutrino-radiation hydrodynamics.

*Subject headings:* methods: numerical — neutrinos — radiative transfer — stars:  
massive — stars: neutron — supernovae: general

## 1. Introduction

Neutrinos play an essential role in the mechanism of core-collapse supernovae as a driving force in the dynamics starting from the gravitational collapse of massive stars. Transport of energy and lepton number via neutrinos is particularly crucial to determine their outcomes, i.e. explosions with an energy of  $10^{51}$  erg (Bethe 1990; Kotake et al. 2006; Janka et al. 2007). Electron-type neutrinos are produced by electron captures in the collapsing phase and are trapped inside the central core to give pressure support. Pairs of neutrinos are created after bounce as a part of the thermal energy converted from the gravitational energy. Emissions of the trapped neutrinos result in an energy release of  $\sim 10^{53}$  erg in the form of supernova neutrinos. The release of this huge energy in neutrinos was indeed vindicated in the observed events of SN 1987A (Hirata et al. 1987). The emitted neutrinos carry valuable information of the mechanism of explosion as well as the properties of dense matter inside compact stars and progenitors (see Nakazato et al. (2013), for example, and references therein).

Interactions of neutrinos with material in the supernova core contribute to the energy transfer in a significant size. The shock wave generated by core bounce stalls soon after the launch and fizzles later in the case of strictly spherical geometry. Without such an artificial restriction in geometry, multi-dimensional hydrodynamical instabilities occur and push the stalled shock so that it could hover at larger radii. A portion of the emitted neutrinos is absorbed by the matter behind the stagnant shock wave and may lead eventually to its outward propagation again. This so-called neutrino heating mechanism (Bethe & Wilson 1985) combined with the multi-dimensional hydrodynamical instabilities is one of the most promising ways to trigger the explosion particularly under a marginal condition. In fact,

---

<sup>1</sup>Current address: Institute of Physical and Chemical Research (RIKEN), 2-1 Hirosawa, Wako, Saitama 351-0198, Japan

energy gain by the neutrino heating amounts to  $\sim 10^{51}$  erg, which is comparable to the observed explosion energy of supernovae (Janka & Müller 1996). Whether the neutrino heating mechanism is the essential cause of explosion or not remains an unsolved issue, though (Janka et al. 2012; Burrows 2013).

In order to advance further our understanding of the role of neutrinos in the intrinsically multi-dimensional dynamics, the evaluation of neutrino heating and cooling should be as accurate as possible. Neutrinos interact with matter very frequently and diffuse outward only gradually inside the proto-neutron star just born after the bounce. Since the temperatures are high in the proto-neutron star, neutrinos are coolant there. On the other hand, a partial absorption of the emitted neutrinos takes place outside the neutrino-sphere below the stalled shock wave before they stream out of the star freely, which heats the matter there.

Quantitatively accurate treatment of neutrino transfer is hence mandatory to provide correct rates of cooling and heating since the energy transport proceeds across the region, where neither diffusion nor free-streaming approximation is applied. The emergent fluxes and energy spectra of neutrinos are determined by the neutrino-matter interactions around the energy-dependent neutrino-spheres. We need to do multi-energy group computations, since the interactions strongly depend on the neutrino energy. In the evaluation of the heating rate, on the other hand, the local number density of neutrinos are important in addition to the energy spectra. It is hence the angular distributions of neutrinos in their momentum space that should be given precisely. Although they are isotropic near the center and become forward-peaked at large radii, the angular distributions are highly non-trivial in the transitional region, which includes the heating region.

The treatment of neutrino transfer should, therefore, be as accurate as possible, particularly in the description of the energy and angle distributions. In most of

multi-dimensional numerical simulations of supernovae, however, some approximations are employed at the moment. This is simply because the full description of neutrino distributions is a six-dimensional (three spatial coordinates and three momenta of neutrinos) problem, which is formidable even for modern supercomputing resources. While computations with the multi-energy groups are becoming a standard nowadays, angular distributions are still commonly approximated one way or another. Since such approximations can be eliminated in spherically symmetric simulations, the influences of the approximations have been extensively studied (Janka 1992; Messer et al. 1998; Yamada et al. 1999; Liebendörfer et al. 2005). It is well known that the diffusion approximation with a flux-limiter tends to overestimate the degree of forward-peak and thus underestimate the heating rate (Janka 1992; Messer et al. 1998). Although the difference is not so drastic, such a small change may be crucial, tipping the balance for explosion particularly in the marginal conditions (Janka & Müller 1996).

Validation of the approximate methods in multi-dimensions has growing importance, since the post-shock conditions obtained in multi-dimensional simulations appear more marginal for successful explosion. The diffusion approximations (including its variants such as IDSA) and/or the ray-by-ray methods are frequently used in the currently state-of-the-art 2D/3D simulations (Suwa et al. 2010; Müller et al. 2012; Bruenn et al. 2013; Takiwaki et al. 2012; Hanke et al. 2013; Nakamura et al. 2014; Suwa et al. 2014; Bruenn et al. 2014). Although they have reported a considerable number of successful explosions produced by the neutrino heating combined with the neutrino-driven convection and/or the standing accretion shock instability (SASI), their approximate treatments of neutrino transfer introduce a certain level of uncertainty. The influences of these approximations should be examined carefully before drawing any conclusion.

In the past years we have indeed seen the multi-dimensional treatment of neutrino

transfer progress substantially, keeping pace with the rapid increase of supercomputing resources. In two dimensions, multi-angle and multi-energy groups neutrino radiation-hydrodynamics have been performed to follow the post-bounce evolution of supernova cores (Livne et al. 2004; Ott et al. 2008; Brandt et al. 2011). They adopted the discrete-ordinate ( $S_n$ ) method to fully describe angle distributions in 2D space (Livne et al. 2004). Ott et al. (2008) reported the comparisons with the diffusion approximation. They demonstrated that the multi-angle transport is needed to describe the neutrino distributions in globally aspherical supernova cores. Brandt et al. (2011) analyzed further the neutrino heating and showed that the multi-angle transfer leads to less lateral variations in the neutrino distributions owing to an averaging effect. Such a detailed study has been limited to 2D.

In three dimensions, there has been a remarkable progress in the multi-energy group transport, but not in the multi-angle group transport (Takiwaki et al. 2012; Hanke et al. 2013; Takiwaki et al. 2014b; Tamborra et al. 2014; Mezzacappa et al. 2014; Horiuchi et al. 2014). These simulations commonly adopted the ray-by-ray approximations although the radial transport was treated differently: the isotropic diffusion source approximation (IDSA) is employed by Takiwaki et al. (2012, 2014b) whereas the moment equations are solved together with a variable Eddington factor obtained from the solution of the 1D model Boltzmann equations in Hanke et al. (2013); Tamborra et al. (2014). Results obtained by the two groups differ in many respects, most notably on the success or failure of explosion (see e.g. their  $11.2M_\odot$  model). Note, however, that the origin of the differences might be the employed neutrino reactions (Takiwaki et al. 2014a). Provided that the number of reported models is still small and the employed physics and numerics are considerably different among them, it is still premature to draw a firm conclusion from these 3D simulations and further studies should be done systematically with the assessment of the influences from the approximations in 3D neutrino transfer.

The purpose of this study is hence to explore the basic features of 3D neutrino transfer in realistic supernova cores with the multi-angle and multi-energy group Boltzmann solver for the first time. Adopting a set of profiles from 3D numerical simulations by Takiwaki et al. (2012); Horiuchi et al. (2014); Takiwaki et al. (2014a), we run our newly developed code (Sumiyoshi & Yamada 2012) to obtain stationary neutrino distribution functions for those fixed matter configurations. Taking advantage of the multi-angle treatment of our code, we explore the non-radial (polar and azimuthal) transport in the globally and locally aspherical matter distributions. Note that in our previous paper (Sumiyoshi & Yamada 2012) the background models were constructed by artificially deforming spherically symmetric models. We pay particular attention to the behavior of the angle moments of neutrino distribution functions in the transitional regime, which will be useful for development of numerical codes using the moment formalism.

Employing our Boltzmann code, we can study the quality of the ray-by-ray approximation, which is routinely used in many simulations in 2D and 3D<sup>2</sup>. As a matter of fact, simply dropping the polar and azimuthal advection terms, we can emulate the ray-by-ray approximation without changing other settings. We examine the non-radial transport, which will not be fully described in the ray-by-ray approximation. As we will show, the contributions of polar and azimuthal fluxes are significant even outside the optically thick region. It is also found that the ray-by-ray approximation tends to exaggerate the contrast between different radial rays, which may affect local neutrino-heating rates.

The paper is organized as follows. We describe the methodology in §2.1. The realization of the ray-by-ray approximation in our code is also explained there. The 3D profiles taken from Takiwaki et al. (2012); Horiuchi et al. (2014); Takiwaki et al. (2014a) are presented in

---

<sup>2</sup>Some simulations implemented the ray-by-ray plus approximation, in which the lateral coupling is partially taken into account.

§2.2. We report in §3.1 the basic features of 3D neutrino transfer, showing density, radial and non-radial fluxes obtained by the 6D Boltzmann solver. The corresponding results by the ray-by-ray approximation are presented in §3.2 for comparison. We investigate the heating rates obtained by both the 6D Boltzmann solver and the ray-by-ray approximation in §4.1. In §4.2, we present the results for other profiles and demonstrate that our findings are generic. The volume-integrated heating rates are examined in §4.3 to discuss the global influences of 3D neutrino transfer on the supernova dynamics. In §5, we show the angle and energy moments of the neutrino distribution functions. Discussions and implications of our study are given in §6 followed by the summary in §7.

## 2. Numerical settings

### 2.1. Neutrino transfer in 3D space

We adopt the numerical code to solve the Boltzmann equation in 6D (Sumiyoshi & Yamada 2012). The code solves the time evolution of the 6D neutrino distribution functions in the spherical coordinate system by using neutrino energy and two angles to designate the neutrino momenta. The 6D Boltzmann equation in the conservative form is discretized in a finite-differenced method on a spatial grid as well as multi-energy and multi-angle grids. We employ the discrete-ordinate ( $S_n$ ) method to describe the angular distributions. The implicit differencing is adopted for the advance of time step to solve stiff equations and to ensure the stability for the equilibrium solution. Further details of the numerical scheme can be found in Sumiyoshi & Yamada (2012).

A basic set of the neutrino reactions is implemented in the collision term (Bruenn 1985; Sumiyoshi et al. 2005). The set includes the emission, absorption and scattering of neutrinos via nucleons and nuclei. The pair processes via electron-positron annihilation,

creation and the nucleon-nucleon bremsstrahlung are also taken into account. We treat the three neutrino species,  $\nu_e$ ,  $\bar{\nu}_e$  and  $\nu_\mu$ . The last one is actually a representative of four species,  $\nu_\mu$ ,  $\bar{\nu}_\mu$ ,  $\nu_\tau$  and  $\bar{\nu}_\tau$ <sup>3</sup>. It is to be noted that the densities, fluxes and angle moments of  $\nu_\mu$  is for one species whereas the contributions of the four species are summed for the cooling and heating rates. The same setting has been used in our previous paper (Sumiyoshi & Yamada 2012) for detailed comparisons with the 1D results of core-collapse supernovae from Sumiyoshi et al. (2005). These neutrino reactions are the most important but certainly not sufficient. The electron-neutrino scattering, for example, is omitted in the current study (Thompson et al. 2003; Burrows et al. 2006). This is mainly due to the limitation of numerical resources and modernization will be definitely needed (Lentz et al. 2012a). The equation of state of Lattimer & Swesty (1991) are used for all calculations in the current study so that better consistency would be obtained with the profiles we adopt from the supernova simulations by Takiwaki et al. (2012); Horiuchi et al. (2014); Takiwaki et al. (2014a).

We follow the time evolution of the neutrino distribution functions by the 6D Boltzmann solver for the fixed background profiles until stationary states are reached (typically in  $\sim 20$  ms) from arbitrarily set initial conditions, in which essentially no neutrino exists. We ignore fluid motions although the original numerical data include such information. We neglect all the velocity-dependent terms in the current study and do not distinguish the inertial frame from the fluid-rest frame, since our aim here is to understand the basic 3D features of the neutrino transfer. It should be emphasized, however, that these velocity-dependent terms in the Boltzmann equation cannot be neglected in more realistic simulations as demonstrated by Lentz et al. (2012b). As a matter of fact, the implementation of all the

---

<sup>3</sup>This group is often denoted by  $\nu_x$  or  $\nu_{\mu/\tau}$  and is sometimes used to show the summed contributions of four species.

velocity-dependent effects to the current Boltzmann solver has been already done and its application to 2D neutrino-radiation hydrodynamics simulations is currently under way (Nagakura et al. 2014).

In addition, we perform approximate calculations by a ray-by-ray prescription in our framework by dropping off the advection terms for spatial  $\theta$ - and  $\phi$ -derivatives as well as neutrino-angle  $\phi_\nu$ -derivative in the Boltzmann equation. We compute the stationary states of the 3D neutrino transfer with the same setting for profiles and reactions. We compare the numerical results by the two methods and examine the differences due to the approximation.

The numbers of spatial grid points employed for neutrino distribution functions are  $N_r = 256$ ,  $N_\theta = 64$ ,  $N_\phi = 32$  for our baseline 3D models. The numbers of neutrino angle ( $\theta_\nu$ ,  $\phi_\nu$ ) and energy ( $\varepsilon_\nu$ ) grids are  $N_{\theta_\nu} = 6$ ,  $N_{\phi_\nu} = 12$  and  $N_{\varepsilon_\nu} = 14$ , respectively. The energy grid points are placed logarithmically from 0.9 MeV to 300 MeV with additional grid points for high-energy tails. Computations with this mesh using 1.6TB memory are the largest scale available on 8 nodes of HITACHI SR16000 at KEK. In order to obtain one configuration of the model by the time evolution in several tens of milliseconds, we need a run of  $\sim 4 \times 10^4$  steps using the MPI-parallel code of the 6D Boltzmann solver. It typically takes  $\sim 200$  hours of wall-clock time on 8 nodes of SR16000 by 128 MPI processes.

Although the current setting of the angle and energy grids is sufficient to obtain the reasonable results as validated by the convergence test in Sumiyoshi & Yamada (2012), we have additionally studied the convergence by increasing the number of grid in some sample models. For this purpose, we perform the numerical simulations for the inner part of the supernova core ( $\leq 360$  km) using  $N_r = 128$  and increase the angle resolution. When we increase  $N_{\theta_\nu}$  from 6 to 8, we find typical differences within 2 % in the neutrino densities, fluxes and heating rates. In the case of increasing  $N_{\phi_\nu}$  from 12 to 16, the differences are

within  $\sim 0.8\%$ . Appearance of large differences of the heating rates is limited near the gain radius due to very small values close to zero.

## 2.2. 3D supernova cores

We utilize the post-bounce matter profiles taken from the 3D numerical simulations of core-collapse supernovae by Takiwaki et al. (2012); Horiuchi et al. (2014); Takiwaki et al. (2014a), who followed the evolutions of  $11.2M_{\odot}$  and  $27.0M_{\odot}$  stars of Woosley et al. (2002). Their computations employed the extended ZEUS-MP code for hydrodynamics (Hayes et al. 2006; Iwakami et al. 2008) and the IDSA scheme (Liebendörfer et al. 2009) for neutrino transport with the ray-by-ray approximation. We use the  $11.2M_{\odot}$  model (11M) as the baseline model for detailed analysis. The profiles adopted from this model represent the typical situations, in which the revived shock wave is expanding toward an explosion. On the other hand, the  $27.0M_{\odot}$  model (27M) (Horiuchi et al. 2014; Takiwaki et al. 2014a), which were computed with the improved code and details will be reported elsewhere, does not lead to shock revival and represents the situations in such prolonged stagnations. It is to be noted that since the profiles we use in this study are obtained in the simulations with the ray-by-ray approximation, our results may be somewhat influenced indirectly by the approximation.

We adopt the 3D profiles of density, temperature and electron fraction (but not velocity) from the dynamical simulations and remap them onto our numerical mesh. We use the same radial (logarithmically spaced) grid up to 2600 km as those employed in the simulation of  $11.2M_{\odot}$ . To cover the whole solid angle in space, we deploy the same number of uniform azimuthal grid points as in the dynamical simulation while a different (non-uniform) polar grid is used so that it would fit our Boltzmann solver. We take the same spacial mesh also for 27M, interpolating the density, temperature and electron

fraction. Other thermodynamical quantities are derived from the equations of state by Lattimer & Swesty (1991) with the incompressibility of 180 MeV for 11M and 220 MeV for 27M, respectively, just as in the original simulations.

In Figure 1, we show the 3D profiles of supernova core for the  $11.2M_{\odot}$  star at 100, 150 and 200 ms after the bounce. They correspond to the phase, in which the shock wave expands gradually from  $\sim 300$  km to  $\sim 600$  km in a non-spherical manner. The revival of shock wave occurs earlier (at  $\sim 50$  ms) due to the neutrino heating and its outward propagation is assisted by the enhanced heating through the hydrodynamical instabilities. This 3D model leads to a successful explosion.

We display in Fig. 2 the color maps of the core (11M) on the xy-plane ( $z=0$ ) at 150 ms after the bounce. The shock wave is located around 400–500 km with an elongated shape at  $\phi \sim 45^{\circ}$  and  $\phi \sim 225^{\circ}$ . The low entropy region prevails along  $\phi \sim 135^{\circ}$  and  $\phi \sim 315^{\circ}$ , which correspond to down flows of proton-rich matter. This nearly dipolar configurations may have arisen from the weak  $\pi/2$  periodicity in  $\phi$ , which was planted accidentally in the perturbation imposed initially in the dynamical simulation<sup>4</sup>. The density and temperature distributions of the central object (proto-neutron star) are almost spherical with only the outer layer being deformed. The configurations at other times are qualitatively similar but with elongations at different  $\phi$ -angles.

Figures 3 and 4 show the color maps of entropy and mass fractions of nucleons on the meridian slices at  $\phi=51^{\circ}$  and  $141^{\circ}$ , respectively. Mushroom-like shapes of high entropy regions reflect convective motion and the associated shock dynamics. On the equator, the

---

<sup>4</sup> Takiwaki et al. (2012) indeed added a perturbation pointwise-randomly. The resultant perturbation, however, had a  $\pi/2$  periodicity weakly in the azimuthal direction by accident, which was not mentioned in their paper.

high entropy region extends up to the shock front at  $\phi=51^\circ$  and there is a narrow channel of low entropy matter at  $\phi=141^\circ$ . Free neutrons are abundant close to and inside the proto-neutron star whereas free protons populate rather abundantly at larger radii where the entropy is high. Nucleons behind the shock wave act as chief absorbing material in the neutrino heating.

In Figure 5, we show the 3D snapshots for the  $27.0M_\odot$  model at 150 and 200 ms after the bounce. In the supernova simulation, the shock wave stalls and is hovering around 200 km up to 700 ms. There is no sign of shock revival. Figures 6 and 7 present the color maps of entropy at 150 and 200 ms, respectively, on the xy-plane ( $z=0$ ) and the meridian slice at  $\phi=51^\circ$ . The shape of the stalled shock wave is nearly spherical with a slight deformation due to the convection in the heating region. High-entropy blobs grow and move upward and low-entropy matter falls downward in channels formed between the mushroom-like shapes. The convective motion with the down flows leads to the non-uniform composition in the central core as in Figs. 3 and 4 for the 11M model. We note that there is no periodic pattern in the azimuthal direction in this model.

### 3. Neutrino distributions

#### 3.1. Density and flux by Boltzmann evaluation

We show the 3D features of the neutrino distributions and its associated moments obtained for the snapshots of the 3D supernova core. We mainly display the numerical results for the snapshot of 11M at 150 ms after the bounce. The 3D characteristics of the neutrino transfer shown below are common also for the other snapshots.

We show in Fig. 8 the iso-surfaces of the density of electron-type anti-neutrinos ( $\bar{\nu}_e$ ) with arrows of its flux vector. The distribution of neutrinos is spherical at center, but

deformed in the surrounding region, reflecting the convective high entropy region. The corresponding fluxes are non-radial according to the gradients of the deformed distributions. The distribution further out is again spherical due to the outward neutrino fluxes at large radii. These 3D features are seen also for the densities and fluxes for electron-type neutrinos ( $\nu_e$ ) and  $\mu$ -type neutrinos ( $\nu_\mu$ ).

Figure 9 displays the color maps of the density of neutrinos for three species ( $\nu_e$ ,  $\bar{\nu}_e$  and  $\nu_\mu$ ) on the xy-plane ( $z=0$ ). The  $\nu_e$ -distribution is focused inside the proto-neutron star with high chemical potential of neutrinos. The  $\bar{\nu}_e$ - and  $\nu_\mu$ -distributions are concentrated in the off-center region, where the degeneracy is low due to high entropies. Among the three species, the  $\bar{\nu}_e$ -distribution exhibits the most non-spherical shape. The  $\nu_e$ -distribution is spherical at center and slightly deformed in the surrounding region. They are affected by the non-spherical shape of the degeneracy of neutrinos ( $\eta_\nu = \mu_\nu/T$ ). The  $\nu_\mu$ -distribution is entirely spherical, reflecting the spherical shape of temperature distribution as seen in Fig. 2.

The 6D Boltzmann solver handles the advection in 3D space and, therefore, describes the non-radial advection as well as the radial advection. Figure 10 reveals the three components of the flux of  $\bar{\nu}_e$  on the xy-plane ( $z=0$ ) corresponding to Fig. 9. There are significant contributions of polar ( $\theta$ ) and azimuthal ( $\phi$ ) fluxes due to the deformed  $\bar{\nu}_e$ -distribution. The direction of the flux follows roughly the gradient of neutrino distribution in the central region. The magnitude of the non-radial component of the flux reaches more than 50 % of the radial component around 20–50 km inside the proto-neutron star.

The 6D Boltzmann solver enables the seamless description of non-radial fluxes in the wide region while the diffusion approximation is applicable only under the optically thick condition. The non-radial fluxes remain significant up to large radii, going out the optically thick region. The neutrino transport is diffusive well inside a radius of 50 km

and transitional to the free-streaming around 100 km as we will see that the second angle moment,  $\langle \mu_\nu^2 \rangle$ , is less than 0.35 inside 50 km in Figs. 33 and 35.

Figure 11 shows the neutrino densities for three species in the central region on the meridian slices at  $\phi=51^\circ$  and  $141^\circ$ . The deformed shapes of density distributions are seen for  $\nu_e$  and  $\bar{\nu}_e$  while the shape is spherical for  $\nu_\mu$  as we saw in Fig. 9. The  $\bar{\nu}_e$  and  $\nu_\mu$  are abundant in the off-center region due to their origin of thermal production and the neutrino degeneracy for the former. There is a bump around the equator in the case of  $\phi=141^\circ$  for  $\nu_e$  and  $\bar{\nu}_e$ . This corresponds to the narrow channel with the proton-rich and low entropy condition seen in Fig. 4. The production of neutrinos is amplified by local enhancement of thermodynamical quantities, which we discuss later.

Prominent non-radial fluxes of  $\nu_e$  and  $\bar{\nu}_e$  can be seen in Figs. 12 and 13, where the three components of flux are shown on the meridian slices. The polar component exhibits fine structure with alternating directions and the azimuthal component widely extends. It is remarkable to see that the directions of flux for  $\nu_e$  and  $\bar{\nu}_e$  are opposite each other. This is because the neutrino chemical potential and temperature (and their gradient) affect the distributions of two species in an opposite way. (See Fig. 14 and discussion below) The flux for  $\nu_\mu$  is almost spherically symmetric (not shown here) and its radial flux is concentrated around its off-center density distribution. The magnitude of the non-radial fluxes is comparable to that of radial flux in some regions. Its ratio to the magnitude of the radial flux reaches more than 50 % around the central object up to  $r \sim 40$  km. The non-radial fluxes extend up to 100 km for  $\nu_e$  in the case of  $\phi=141^\circ$ . This corresponds to the narrow region near the equator noted above.

As we have seen, the neutrino distributions are affected by the neutrino degeneracy. While the temperature distribution is almost spherical, the chemical potential (i.e. degeneracy) shows non-uniform features in the central region inside the neutrino-sphere

and the surrounding region up to the location of the shockwave. We show in Fig. 14 the temperature, neutrino chemical potential and neutrino degeneracy on the meridian slices corresponding to Figs. 11, 12 and 13. Having a deformed shape in the profile of electron fraction, the distribution of the neutrino chemical potential is non-spherical. We overlay the location of the neutrino-sphere for the neutrinos with an energy bin of  $E_\nu = 34$  MeV for three species. Here the neutrino-sphere is defined by the location where the optical depth is 2/3 along the radial coordinate. For this purpose, we evaluated the optical depth by using the opacities for the neutrinos in the forward angle bin.

In the outer layer, the neutrino distributions become rather spherical due to an averaging effect by the integration of neutrino fluxes from various angles while the neutrino distributions are inhomogeneous in the central region. This is the characteristics of the 6D Boltzmann solver to describe the advection in 3D space. This finding is in accord with the result found in 2D space by Ott et al. (2008). We will demonstrate characteristics of the ray-by-ray approximation in 3D through comparisons with the 6D Boltzmann results in the following sections.

The deviations from the spherical shape even in the outer layer occur in the case of  $\phi=141^\circ$  due to a spot in the narrow channel near the equator. In this region, the neutrino-spheres of  $\nu_e$  and  $\bar{\nu}_e$  pass through the degenerate regime, i.e. low temperature and high neutrino chemical potential. This spot effect is evident in densities and fluxes for  $\nu_e$ , modest for  $\bar{\nu}_e$  and not discernible for  $\nu_\mu$ . This order corresponds to the positions of neutrino-sphere for three species from outside toward the center. In the case of  $\phi=51^\circ$ , variations of neutrino degeneracy around the neutrino-spheres are not drastic, therefore, leading to rather spherical distributions in the outer layer besides non-uniform distributions at center. We see these two types of behavior in non-uniform situations depending on positions and timing in the models. The spot effect may cause enhanced/reduced neutrino

distributions and associated changes of heating rates as we will examine below.

### 3.2. Density and flux by ray-by-ray evaluation

In this section, we demonstrate by comparison between the full Boltzmann transport and the ray-by-ray approximation that the latter tends to exaggerate asymmetries outside the neutrino-sphere. The relative difference of a quantity  $Q$  between the two methods is hereafter denoted by  $\delta_Q = (Q_{RbR} - Q_{Boltz})/Q_{Boltz}$ , where  $Q_{RbR}$  and  $Q_{Boltz}$  are the values of  $Q$  obtained by the ray-by-ray and Boltzmann evaluations, respectively. As already mentioned, the background models employed in the current study were obtained with the ray-by-ray approximation and the following results may be somewhat affected indirectly.

In Fig. 15, we display the densities of  $\nu_e$  and  $\bar{\nu}_e$  on the xy-plane obtained for the 11M model at 150 ms by the two methods. The relative difference between them is also shown in the bottom panels. The distribution is not spherical even in the outer region ( $> 100$  km) for the ray-by-ray evaluation. This is the artifact of the ray-by-ray approximation. The neutrino fluxes are mainly determined by the environment around the neutrino-sphere. In the ray-by-ray approximation, the local enhancement (or suppression) of neutrino fluxes at a particular point on the neutrino-sphere due to variations of temperature and/or chemical potential are propagated along the radial ray that emanates from the point alone. In reality, however, neutrinos move also in other directions and affect the densities and fluxes on different radial rays. In the absence of such a mixing among different radial rays, the ray-by-ray approximation exaggerates the contrast among different rays as shown in the bottom panels.

The same features can be consistently seen in the behavior of fluxes shown in Fig. 16. The distributions of fluxes in the ray-by-ray approximation have non-spherical features in

the outer region due to enhancement or reduction along the radial rays. In some cases, the difference of  $\nu_e$  flux has anti-correlation with that of  $\bar{\nu}_e$  flux. When the neutrino chemical potential is high at the neutrino-sphere in one ray, the  $\nu_e$  flux is enhanced along the ray but  $\bar{\nu}_e$  flux is suppressed. Although the neutrino fluxes for two species may depend on the location of neutrino-spheres, the environment and other factors, we find that these features often appear in many profiles of our models as we will show.

We demonstrate that the anisotropy in the ray-by-ray approximation can be large enough to affect the densities and fluxes at large distances, depending on the position. Fig. 17 shows the neutrino densities obtained by the ray-by-ray approximation on the meridian slices, which corresponds to the ones in Fig. 11. The neutrino densities of  $\nu_e$  and  $\bar{\nu}_e$  are not spherical at  $\sim 100$  km in contrast to the spherical shape found in the 6D Boltzmann evaluation. In the case of  $\phi=141^\circ$ , the anisotropy around the equator is enhanced more than that in the 6D Boltzmann evaluation. We display the relative difference between the two methods in Fig. 18. Depending on the polar direction, there are regions of overestimation or underestimation of densities for  $\nu_e$  and  $\bar{\nu}_e$  in the outer region. The enhancement (or reduction) at the emission region persists along the ray due to the averaged radial propagation of neutrinos. There is anti-correlation between the two species ( $\nu_e$  and  $\bar{\nu}_e$ ) in the differences along the ray. This is again because the emission is determined by the neutrino degeneracy, which enhances and reduces the flux of  $\nu_e$  and  $\bar{\nu}_e$ , respectively.

The anisotropy of densities arises from angular variations of the fluxes of neutrinos emitted from the region of neutrino spheres. We show the behavior of neutrino fluxes in Figs. 19 and 20 for the two meridian slices at  $\phi=51^\circ$  and  $141^\circ$ , respectively. The relative differences of the ray-by-ray evaluation from the 6D Boltzmann evaluation are also displayed for each profile in the right panels. One can clearly see the overestimation or underestimation of the fluxes along the radial ray, depending on the polar angle. The

anti-correlation between the two species appears apparently on the two slices as seen in the profiles on the  $xy$ -plane in Fig. 16. The pattern of differences in the flux corresponds to that in the densities shown in Fig. 18. In the case of  $\phi=141^\circ$ , the differences are large for both species in a wide region. The region around the equator has a significant deviation due to the narrow channel.

We further examined the variations of the neutrino distributions and the anti-correlation between the two species. We show the polar angle dependence of quantities at the fixed radius on the meridian slice at  $\phi=51^\circ$  in Figs. 21 and 22. The neutrino densities are well determined by the local environment (temperature and neutrino chemical potential) in the optically thick region at radius of 54 km in Fig. 21. We see the neutrino densities follow the variation of the neutrino chemical potential while the anti-neutrino densities have the anti-correlated variation.  $\mu$ -type neutrinos have a constant distribution since the temperature stays almost constant. Both the two evaluations provide the neutrino distributions simply reflecting the environment. The ray-by-ray evaluation shows slightly stronger variations than the 6D Boltzmann evaluation.

Neutrino distributions become different from the variation of local environment as we leave the the optically thick region and go further away from the region of the neutrino-sphere. At radius of 94 km in Fig. 22, the neutrino densities by the 6D Boltzmann evaluation become more flat than the variations in the neutrino chemical potential. This is due to the averaging effect by the non-radial fluxes. In contrast, the neutrino densities by the ray-by-ray evaluation show clear variations due to the degeneracy, keeping the anisotropy produced deep inside the core. The anti-correlation between the two species remains similar to the situation at the inner position. As shown in these examples, the non-uniform distribution of neutrino chemical potential inside the core is important to determine the neutrino distributions in the outer region. Note that the electron fraction is

a key factor to determine the neutrino chemical potential even when the distributions of density and temperature are spherical inside the core.

#### 4. Evaluation of energy transfer rates

In this section, we examine the heating rates in the supernova core by the 6D Boltzmann solver. Since the heating rate is a crucial quantity to explore the neutrino heating mechanism, we investigate also the heating rates obtained by the ray-by-ray approximation so that we can assess possible differences due to the approximation popularly used in multi-dimensional simulations. We show that differences of the heating rate occur along the radial ray due to the ray-by-ray approximation in the same way as those found above. The size of differences depends on the environment around the neutrino-sphere, which provides the differences in the densities and fluxes.

##### 4.1. Heating rates by Boltzmann and ray-by-ray evaluations

We describe here the behavior of the heating rates by the two methods in the supernova core of 11M at 150 ms after the bounce. We display the heating rates on the xy-plane in Fig. 23 by the 6D Boltzmann (top) and ray-by-ray (middle) evaluations. The relative differences of the ray-by-ray evaluation with respect to the 6D Boltzmann evaluation are also shown in the bottom panel. While the profiles of heating region in red are similar each other, there are two spots with enhanced heating rates in the ray-by-ray evaluation. Along the two directions, the ray-by-ray approximation leads to the overestimation of  $\sim 20\%$ . This enhancement corresponds to the enhanced densities and fluxes shown in Figs. 15 and 16 and is caused by the inhomogenous distributions of neutrino degeneracy with the *hot spot* for neutrino emissions as discussed above. There are also regions of minor differences

along some radial directions. Note that large differences near the gain radius in the central part appear since the energy transfer rate is very small there.

Figure 24 displays the profiles for the neutrino-heating rate on the meridian slices at  $\phi=51^\circ$  and  $141^\circ$  corresponding to Fig. 23. The heating rates by the 6D Boltzmann (left) and ray-by-ray (middle) evaluations are shown along with the relative differences of the ray-by-ray evaluation (right). In the case of  $\phi=51^\circ$ , there is no noticeable difference in the heating rates between the two methods except for a slight underestimation along two directions. A significant overestimation is seen around the equator in the case of  $\phi=141^\circ$ . This corresponds to the one of the azimuthal directions with overestimation seen in Fig. 23. The overestimation in the ray-by-ray approximation occurs due to the enhanced neutrino fluxes in the narrow channel. There are also wide areas with overestimation and a radial direction with underestimation in the heating region.

While the differences of the *total* heating rate appear in the limited directions, those of each heating rate for major reactions generally occur in the whole region. In Figure 25, we show the heating rates and their relative differences between the two methods for  $\nu_e$  and  $\bar{\nu}_e$  absorptions on nucleons on the meridian slice at  $\phi=51^\circ$ . One can see the pattern of enhancement or reduction of the individual heating rate just in the same way as those in the densities and fluxes. On the one hand, significant differences with an alternate sign appear along the radial ray for the  $\nu_e$  absorption in the upper panel. This pattern arises from the differences of  $\nu_e$  fluxes seen in Fig. 19. On the other hand, differences of the similar size for the  $\bar{\nu}_e$  absorption appear in the same pattern but with a different sign. This pattern reflects the corresponding pattern for  $\bar{\nu}_e$  in Fig. 19. Due to the production mechanism of the fluxes for two species, the overestimation and underestimation of the heating rates arise in the opposite way. Therefore, the total heating rates do not have large differences in most of the regions due to cancellation. This mechanism of the cancellation of the two heating rates is

generally seen in our analyses of the models.

The anisotropy of heating rates in the ray-by-ray approximation may have influences on the hydrodynamics in multi-dimensions. The enhancement of heating beamed along a certain direction may lead to the modification of shock dynamics. In contrast, the 6D Boltzmann evaluation provides mildly anisotropic distributions of the neutrino heating by the integration from various angles. We remark here that the anisotropy in the ray-by-ray approximation is found in the fixed hydrodynamics. It is necessary to examine whether these features persist for a long time scale in dynamical situations by neutrino-radiation hydrodynamics (See also §4.3.2).

## 4.2. Heating rates in other profiles

We explore generic characteristics of the heating rates by examining the profiles at different timing and models. We demonstrate that the characteristic differences along the radial ray due to the ray-by-ray approximation occur also in the other cases. Their magnitude and sign, however, vary depending on the environment.

### 4.2.1. Different snapshots of 11M

The heating rates at 100 ms after the bounce by the 6D Boltzmann evaluation are shown in Figs. 26 and 27 together with the relative differences of the ray-by-ray evaluation. One can see, in Fig. 26, the deformed shape of the heating region and the underestimation of the heating rate in the ray-by-ray evaluation widespread on the xy-plane, being independent of  $\phi$ -direction, with a fluctuating size. In Fig. 27, the overestimation of the heating rate occurs around the z-axis within a wide polar angle while the underestimation is confined around the equator.

The pattern of differences looks differently, depending on the environment. We show the case at 200 ms in Figs. 28 and 29. The deviations alternately appear depending on the  $\phi$ -direction on the xy-plane as seen in Fig. 28. They depend on the polar angle and there are large variations on the meridian slice in Fig. 29. While the underestimation with a large magnitude appears in the limited region along a certain direction in the case of  $\phi=51^\circ$ , significant overestimation appears at two polar directions on the meridian slice at  $\phi=141^\circ$ . These beam-like structures resemble the situation in the case of  $\phi=141^\circ$  at 150 ms. In fact, the neutrino degeneracy around the neutrino-sphere is locally high at the two spots, which lead to high neutrino fluxes and, therefore, heating rates. These spots are located around a narrow channel between the two mushroom-like flows like the case for 150 ms.

#### 4.2.2. Snapshots of 27M

We examine the heating rate for the 27M models in order to find the generic characteristics of the ray-by-ray approximation. In contrast to the 11M models considered so far, the shock wave in this model remains stagnated and does not show any hint of shock revival until the end of the simulation ( $\sim 700$  ms), which is consistent with other group's results (Hanke et al. 2013; Tamborra et al. 2014). This model is a representative of those models, which seem to be most difficult for the neutrino heating to produce explosions, and will hence serve our purpose here.

We found that differences between the ray-by-ray approximation and the full Boltzmann treatment are no less significant in this case. We show the heating rates as well as the relative differences at 150 and 200 ms after the bounce in Figs. 30 and 31. The upper panels display the heating rates obtained by the 6D Boltzmann solver on the xy-plane and the meridian slice at  $\phi=51^\circ$ . The lower panels present the relative differences of the ray-by-ray evaluation. One can see that the differences are conserved along radial rays, i.e., over- and

underestimations occur as radial beams just as in the 11M models. The deviations are substantial in the heating region, particularly near the gain radius, but remain beyond the shock wave located at  $\sim 200$  km. We confirm that this behavior is generic and is observed for other slices. When there is a hot spot on the neutrino-sphere that the down flow of proto-rich matter hits, then the ray-by-ray approximation tends to propagate the local enhancement in the neutrino density along the radial ray that emanates from the spot. These generic features of the ray-by-ray approximation may have non-negligible influences on the revival of the stalled shock wave and should be carefully assessed further.

### 4.3. Volume-integrated heating rates

Since we found that the heating rates are locally different, it is of great importance to examine the total amount of the heating rate by the 6D Boltzmann solver and the ray-by-ray approximation. We evaluate the volume-integrated heating rates in the two evaluations to check this point. The specific heating rates, which we have discussed in the previous sections, are defined by

$$q_\nu = - \int d\Omega E_\nu^2 dE_\nu E_\nu \left( \frac{\delta f}{\delta t} \right)_{collision} , \quad (1)$$

with the collision term in the Boltzmann equation. The total amount of the heating rate is calculated by the integral over the volume in the heating region,

$$Q_\nu = \int dV q_\nu \rho , \quad (2)$$

where  $\rho$  is the mass density. The range of the integral covers the heating region, where the energy transfer is positive. We set the inner boundary of the heating region at the gain radius, where  $q_\nu$  becomes zero along the radial coordinate. We define the outer boundary by the location of the shock wave when the entropy per baryon becomes 5.5 in the unit of the Boltzmann constant,  $k_B$ .

#### 4.3.1. *Snapshots*

In Table 1, we compare the volume-integrated heating rates for the 11M and 27M models in the two evaluations. The volume-integrated heating rates in the ray-by-ray approximation are slightly smaller than the values in the 6D Boltzmann evaluation. The difference is within  $\sim 2\%$  for 11M and less than 1% for 27M. One may wonder the reason why the volume-integrated heating rate by the ray-by-ray approximation is not significantly different from the one by the 6D Boltzmann solver. This is because the overestimation and underestimation of the heating rates in the local regions along the radial ray cancel out by the integral over the solid angle. The current analysis suggests that the local deviations in the ray-by-ray approximation are more influential than the total deviations. It should be noted, however, that even a slight difference in the heating rate can be crucial to the revival of the shock wave in the marginal situation (Janka & Müller 1996). It is necessary to study this influence further by examining the hydrodynamical evolution.

#### 4.3.2. *Time variations*

So far we have discussed the features of stationary neutrino distributions obtained for snapshots that are mutually separated in time by 50 ms. One may argue that rapid temporal changes in matter distributions might erase some of those features by averaging. In order to check this, we perform another series of simulations. We adopt consecutive snapshots from the period of 145 ms to 155 ms with an interval of 1 ms from the same supernova simulation of  $11.2M_{\odot}$  star; there are hence 11 snapshots including the one at 150 ms, which we have already discussed; we then follow the time evolution of neutrino distributions until they become stationary for each time slice and take the average of the results over these 11 simulations. In this way we can judge how sensitive our findings are to the short-time variations of the background.

We show the temporal evolution of the total heating rates during the 10 ms in the two evaluations in Fig. 32. In both cases, there is a gradual decrease owing to the change in hydrodynamical conditions. One can see that the ray-by-ray approximation provides systematically smaller rates than the 6D Boltzmann evaluation over this period. The deviation of the ray-by-ray evaluation stays around  $-2\%$ . This result suggests that the underestimation by the ray-by-ray approximation is not an artifact of the fixed-background models, but a generic feature originated from the nature of the approximation itself. In fact, we find that the local deviations over  $20\%$ , which are seen in Figs. 23 and 24, are also observed in this case and last for  $\sim 10$  ms.

## 5. Angle moments

Various moments of the neutrino distribution function are important to reveal the 3D features of the neutrino transfer. They are also useful to develop new methods for the closure relation in the moment formalism (see Shibata et al. (2011) for example). In principle, we can derive various moments with respect to angle and energy from the obtained neutrino distribution function in six dimensions. As an example, we show the contour maps of the angle moments for three species of neutrinos in Figs. 33 and 35 on the meridian slices at  $\phi=51^\circ$  and  $\phi=141^\circ$ , respectively, for the 11M model at 150 ms after the bounce. The spatial distributions of both the first angle moment or the flux factor,  $\langle \mu_\nu \rangle$ , and the second moment,  $\langle \mu_\nu^2 \rangle$ , are almost spherical with a slight deformation in the central part. Some bumps are seen in the narrow region near the equator on the meridian slice at  $\phi=141^\circ$ . The asymptotic behavior of these angle moments at large radii is consistent with those obtained in the previous studies on the flux factor (Messer et al. 1998; Yamada et al. 1999) and on the basic validation of the 6D Boltzmann code (Sumiyoshi & Yamada 2012).

We further examine the angle moments obtained by the ray-by-ray approximation

through comparisons with the 6D Boltzmann evaluation. In Figs. 34 and 36, we show the relative differences of the angle moments evaluated by the ray-by-ray approximation with respect to the 6D Boltzmann evaluation shown in Figs. 33 and 35. Appreciable deviations of the angle moments arise in some regions where non-radial fluxes are large in the neutrino distributions. The deviations become large up to  $\sim 10\%$  and is comparable to those of the other quantities we have seen. The deviations are very small within  $\sim 3\%$  for  $\langle \mu_\nu^2 \rangle$  on the meridian slice at  $\phi=51^\circ$  where the distribution is almost spherical. On the meridian slice at  $\phi=141^\circ$ , the deviation is significant around the narrow channel near the equator due to the hot spot effect. Alternate deviations of underestimation and overestimation appear depending on the radial direction.

It is profitable to note that we can examine all (diagonal and non-diagonal) elements of the Eddington tensors by the 6D Boltzmann solver. Components of the Eddington tensor show interesting features with non-spherical shapes in some cases. The diagonal elements of the Eddington tensor for the energy bin ( $E_\nu = 34$  MeV) of two species of neutrinos ( $\nu_e$  and  $\bar{\nu}_e$ ) are shown in Figs. 37 and 38 on the two meridian slices for the 11M model at 150 ms. In the case of  $\phi=51^\circ$ , the distributions of the three components exhibit deformed shapes in the outer region ( $\sim 250$  km). In the central part, they have spherical shapes for  $\nu_e$  and non-spherical ones for  $\bar{\nu}_e$ , reflecting their distributions. In the case of  $\phi=141^\circ$ , the non-spherical features of the distribution are prominent in a wide region for the two species. The bumpy structure reflects the non-uniform shape of the central core, which has the narrow channel between the two mushrooms.

In usual situations with nearly spherical shapes, only the diagonal elements are dominant with zero non-diagonal elements. We found that there are some regions where the non-diagonal elements are non-negligible. In Fig. 39, we show, as an example, the color maps of the non-diagonal  $(r\theta)$ ,  $(r\phi)$  and  $(\theta\phi)$ -components for the energy bin ( $E_\nu = 34$

MeV) of  $\nu_e$  on the meridian slice at  $\phi=141^\circ$  in the 11M model at 150 ms. Their magnitude amounts to  $\sim 0.1$  and is not negligible around the channel along the equator.

These non-trivial properties of the Eddington tensors are valuable information to express the anisotropy of neutrino distribution functions in 3D supernova cores. Since the neutrino distribution function is symmetric around the radial coordinate in the ray-by-ray approximation, only the three diagonal components are non-zero and the  $rr$ -component determines the other two  $\theta\theta$  and  $\phi\phi$ -components. Hence, the ray-by-ray approximation loses the information of the non-trivial structure of the Eddington tensor. Further studies on the detailed features of the Eddington tensors obtained by the 6D Boltzmann solver are underway to develop new closure relations for the 3D problems as a separate article.

## 6. Discussions

We discuss here some possible implications of our finding for the supernova mechanism and associated phenomena.

The 6D Boltzmann solver provides a seamless description of the neutrino transfer from optically thick to thin regions in 3D space. Non-radial neutrino transfer occurs in general up to large distances from the center beyond the neutrino-sphere, which can have influences on the convective motions of neutrino-rich matter inside the proto-neutron star as well as the emission properties around the neutrino-sphere. These may in turn affect the neutrino heating in the gain region and ultimately the revival of shock wave.

Although the diffusion approximation can describe the non-radial transfer of neutrinos in the optically thick regime, the transition to the transparent regime is handled by a prescribed flux limiter, which is not easy to justify (Janka 1992; Messer et al. 1998). The non-radial neutrino flux at large radii in the semi-transparent and transparent

regimes, which we have seen above, can not be properly described by the diffusion-based approximation, since the flux in these regimes is not determined by the local gradient of neutrino density but is obtained non-locally as a superposition of neutrinos flying in different directions from distant points. The 6D Boltzmann treatment is a unique solution to treat such circumstances rigorously. It is, of course, more desirable to conduct the neutrino-radiation hydrodynamics simulations, which will be a future work, though.

A recent study by the multi-energy group flux-limited diffusion approximation in 2D reported non-explosions for 12–25 $M_{\odot}$  stars (Dolence et al. 2014), being different from the successful 2D simulations by other groups (Suwa et al. 2010; Müller et al. 2012; Bruenn et al. 2013; Nakamura et al. 2014; Suwa et al. 2014). This example again casts a light on uncertainties due to different approximations in neutrino transfer, which might lead to totally different outcomes. The 6D Boltzmann code will be helpful to decipher the discrepancies among them. (See Liebendörfer et al. (2009) for the validation of IDSA in 1D. )

The comparison of the ray-by-ray approximation with the 6D Boltzmann evaluation is beneficial for the supernova research, since this approximation is routinely used for the currently state-of-the-art numerical simulations in 2D and 3D spatial dimensions but its validation is rather scarce. While the ray-by-ray approximation is an efficient way to handle the neutrino transfer in multi-dimensions, it inevitably neglects some of the non-radial neutrino transport (See Buras et al. (2006) for partial coupling) and, as a consequence, tends to enhance artificially the contrast among different radial rays. These features found by the 6D Boltzmann solver in this paper are in accord with the comparison in 2D between the Boltzmann transport and the flux-limited diffusion approximation by Ott et al. (2008) and Brandt et al. (2011) (See also Dolence et al. (2014) for the discussions with a formal solution). It remains to be seen if this effect persists in 3D dynamical simulations.

If the artificial enhancement of neutrino anisotropy lasts for a long period, it may have impact on the hydrodynamics. We have actually seen that it lasts at least for  $\sim 10$  ms. A larger neutrino-heating rate along a certain radial ray will give a strong push to the stalled shock wave locally in that direction. The opposite situation can arise in another direction, where neutrino heating is suppressed erroneously. The ray-by-ray approximation, therefore, may enhance the deformation of shock wave and might induce stronger hydrodynamical instabilities. In the 6D Boltzmann treatment, such anisotropies tend to be smoothed by the non-radial transport. It is advisable to pay an appropriate attention to this effect when one studies the anisotropy of neutrino distributions produced by local matter inhomogeneities.

It remains to be seen whether the improvement by the 6D Boltzmann treatment indeed changes the behavior of hydrodynamical instabilities such as SASI (Blondin & Mezzacappa 2007; Iwakami et al. 2008; Nordhaus et al. 2010; Hanke et al. 2012; Takiwaki et al. 2012; Hanke et al. 2013). Very recently Tamborra et al. (2014) reported with the ray-by-ray approximation a new instability named Lepton-number Emission Self-sustained Asymmetry (LESA), which produces self-sustained, globally dipolar configurations. Note, however, that Dolence et al. (2014) have found no such instability with the flux-limited diffusion approximation. LESA may hence be an artifact of the approximation. In fact, since it is claimed that the global coupling of anisotropy between the neutrino-sphere and shock wave is the key to the instability, accurate evaluations of the neutrino anisotropy may be crucial. It is hence interesting to see what the Boltzmann transport would produce. It may be that eventually only by performing full neutrino-radiation hydrodynamics simulations with Boltzmann transport can we disentangle this new twist.

Our results suggest that the errors by the ray-by-ray approximation may be moderate for most of the cases. This will be a good news for the supernova research in 3D, since the current supercomputing resources are limited and allow only the 3D simulations with

an approximate neutrino transfer. In future, however, it is necessary to remove even such moderate uncertainties. In fact, even a  $\sim 10\%$  error in the heating rate may have an impact on the revival of shock wave particularly when it is marginal.

The neutrino distributions in the transparent regions are determined not locally but globally as a superposition of neutrinos flying in different directions from various distant points. The Boltzmann solver can fully take this into account in sharp contrast to other approximate methods. The neutrino spectra are also affected by such non-local features in neutrino transfer, reflecting thermodynamical states not just at a single point but in a wide region on the neutrino-sphere. It may hence be possible that the Boltzmann solver reveals new features in the neutrino spectra. It would then be also interesting to examine its influences on the nucleosynthesis of heavy elements via neutrino processes.

This will be particularly the case when the proto-neutron star is strongly deformed due to rapid rotation. Since the core is globally asymmetric, the resulting fluxes are intrinsically non-radial. Such an effect was pointed out by Ott et al. (2008) in the case of a rapidly rotating 2D supernova core. Its observational consequences were studied (Brandt et al. 2011). In the case of 3D the neutrino-sphere may be globally non-axisymmetric if the core rotates very rapidly. It would be interesting then to study its possible observational implications with the 6D Boltzmann transport.

The main limitation of the current Boltzmann code is the angular resolution in describing the forward-peaked neutrino distribution functions in the optically thin region. A large number of grid points would be required if one were to fully resolve such configurations, which is simply unaffordable. Fortunately, the area, which we are most concerned with and where the Boltzmann solver is most needed, is the region from beneath the neutrino-sphere up to the stalled shock wave and the neutrino distribution function is not so forward-peaked yet there; the moderate angular resolution we can afford will be acceptable particularly

for the evaluations of heating and cooling rates although detailed convergence tests are certainly necessary. If one wants to obtain the neutrino luminosities and spectra at different viewing angles quantitatively, one may need a finer angular mesh, which may require prohibitive computing resources in the current approach. (See, however, §4 in Kotake et al. (2012) for the scaling of computational load. ) It would then be necessary to develop alternative techniques such as the variable angle mesh (Yamada et al. 1999) or the Monte Carlo method (Abdikamalov et al. 2012).

Although the current study employs only the snapshots from the 3D supernova simulations with the ray-by-ray IDSA (Takiwaki et al. 2012, 2014b; Horiuchi et al. 2014; Takiwaki et al. 2014a), it is desirable to investigate other background models, since the neutrino transfer may be somewhat affected indirectly by the approximation employed in the supernova simulations. It will be also preferable to study the influences of the numerical grid employed (ex. spherical-polar vs 3D-cartesian as well as its resolution) and progenitor models. World wide collaborations will be indispensable in order to fully understand the 3D neutrino transfer. It may become possible then to choose suitable tool for a given problem (See Iliev et al. (2006) for the cosmological radiative transfer codes, for example). The validation of the approximate methods currently used in 3D supernova simulations will be a necessary first step in that direction.

The Boltzmann solver can be combined with the magneto-hydrodynamical code with no problem to study magneto-hydrodynamics scenarios of core-collapse supernovae in more realistic settings. The application will not be limited to the supernova. The neutrino transfer in the collapsar, which originates from more massive stars, for example, will be important for the jet formation in the gamma ray burst. The Boltzmann transport is particularly suitable to study such highly anisotropic and non-local problem. In particular information on the angle moments of neutrino distribution functions will be very helpful to

develop a closure relation for the moment formalism, another approximate method. These issues are now under investigation with the 6D Boltzmann solver and will be reported elsewhere.

Improvements of the current 6D Boltzmann code are certainly needed and may somewhat change the results. Among other things, the implementation of the modern reaction rates instead of the conventional set is mandatory to investigate the post-bounce dynamics quantitatively further as demonstrated in the previous papers (Buras et al. 2006; Lentz et al. 2012a). The modifications of the emission and absorption rates affect directly the cooling and heating rates. Addition of inelastic scatterings of neutrinos will modify their energy spectra and, as a result, anisotropy as well. Even the electron captures on nuclei affect the post-bounce dynamics by setting the initial stage.

The proper account of relativistic corrections is another issue toward the ultimate realism (Liebendörfer et al. 2004; Sumiyoshi et al. 2005; Buras et al. 2006; Lentz et al. 2012b). Implementations of the special relativistic effects such as the Doppler shift and aberration have been actually done recently (Nagakura et al. 2014). Combined with a Newtonian hydrodynamics code, it is now applied to the 2D supernova simulation and the results will be reported elsewhere. The incorporation of general relativistic corrections to the present code is also currently underway (See also Cardall et al. (2013); Shibata et al. (2014)). Its coupling to a general relativistic hydrodynamics code and a solver of the Einstein equation in 3D will be a grand challenge.

## 7. Summary

We have explored the 3D properties of the neutrino transfer in supernova cores by solving the Boltzmann equation in 6 dimensions (3 in space and 3 in momentum space).

We have performed the numerical simulations to obtain the stationary state of neutrino distribution functions in 6D phase space for the fixed backgrounds of the 3D supernova core. We used the typical profiles of the supernova core taken from the 3D supernova simulations of  $11.2M_{\odot}$  and  $27.0M_{\odot}$  stars by Takiwaki et al. (2012); Horiuchi et al. (2014); Takiwaki et al. (2014a). The numerical code to solve the Boltzmann equation in 6D handles the neutrino transfer in multi-energy and multi-angle group for three neutrino species. The three dimensional propagation of neutrinos is described by the  $S_n$  method. The standard set of neutrino reactions is implemented in the collision term together with the table of equation of state.

This is the application of the 6D Boltzmann solver to the realistic profiles of the 3D supernova cores for the first time. The 6D Boltzmann equation directly provides the energy and angle distributions of neutrinos in the whole region of the 3D supernova cores. Most importantly, the transport of neutrinos in the multi-angle description provides the information of the non-radial (polar and azimuthal) directions as well as the radial one. We have demonstrated that the 6D Boltzmann solver describes the 3D features of neutrino transfer, removing the approximations often used in the currently state-of-the-art simulations. The numerical results show that the non-radial fluxes are generally seen inside the proto-neutron star and can extend over the wide region beyond the optically thick region.

We find that the ray-by-ray approximation, which is a popular approximation in the current supernova simulations, provides enhanced directional variations in neutrino distributions. We have computed the 3D neutrino transfer in the ray-by-ray approximation by using our numerical code, dropping off the non-radial transport terms. We have examined the characteristics of the ray-by-ray approximation for the same 3D profiles through the comparison with the 6D Boltzmann evaluation. In the ray-by-ray approximation, the

non-spherical profiles of neutrino densities and fluxes tend to prevail from center to large distances. This is in marked contrast to the 6D Boltzmann evaluation in which the integral from many directions provides the nearly spherical distribution outside the proto-neutron star.

Our analysis has revealed that the ray-by-ray evaluation provides noticeable overestimation or underestimation of densities and fluxes along the radial ray. By examining the relative differences of the ray-by-ray evaluation with respect to the 6D Boltzmann evaluation, the deviations of  $\sim 20\%$  was found to develop depending on the environment. Once the neutrino emission is enhanced due to a local hot spot of the neutrino chemical potential, this modification continues along the radial ray. The reduced neutrino emission is similarly maintained. Therefore, we find alternate distributions of the rays with underestimation and overestimation outside the proto-neutron star. This behavior is seen commonly for  $\nu_e$  and  $\bar{\nu}_e$  distributions, which reflect the non-uniform distribution of the neutrino degeneracy. The sign of the deviations for the two species is opposite each other because of the opposite effects on the emission through the degeneracy.

We have also found that the heating rates evaluated by the ray-by-ray approximation have deviations along the radial ray. The relative differences from the 6D Boltzmann evaluation amount to  $\sim 20\%$  in some regions but smaller than the case of the densities and fluxes in wide regions. This is because the overestimation and underestimation of the heating rates by  $\nu_e$  and  $\bar{\nu}_e$  cancel each other due to their opposite deviations in many cases. Significant deviations occur in the regions where the neutrino degeneracy is prominent from the average distribution, for example, in the narrow channels between the two mushroom-like outflows. This hot spot provides the enhanced heating rate along the particular radial ray. The hot spot effect may last for  $\sim 10$  ms as found in our study using the time series of the profile. We have found that the total amount of heating in the whole

heating region in the ray-by-ray evaluation is slightly smaller than that in the 6D Boltzmann evaluation. These features of the ray-by-ray characteristics are common for the adopted profiles from the  $11.2M_{\odot}$  and  $27.0M_{\odot}$  stars, which represent the exploding and stalled shock situations. Our study calls for careful assessment of the angle-dependent heating effects which may affect the hydrodynamics. We remark that these features are found in the fixed background profiles and further studies in neutrino-radiation hydrodynamics are necessary.

We have examined the basic features of the angle moments and the Eddington tensor in the 3D supernova cores. We show that the angle moments of the neutrino distribution functions obtained by the 6D Boltzmann solver have rather spherical profiles. The relative differences of the ray-by-ray evaluation appear in some regions, but limited within the inner part. The components of the Eddington tensor exhibit deformed distributions in more wide regions than the case of angle moments. Since we have the 6D neutrino distribution functions, we can compute all components of the Eddington tensor and clarify the behavior of the diagonal and non-diagonal elements. We have demonstrated that there are regions with appreciable non-diagonal components in one of the snapshots as an example. Studies of these basic quantities will be helpful to develop new closure relations for the moment formalism in largely deformed profiles such as collapsars.

The current study is a step toward the complete treatment of neutrino-radiation hydrodynamics implementing the full list of neutrino reactions in the general relativistic framework. It is of great interest how the 6D Boltzmann treatment affects the neutrino heating mechanism in hydrodynamical instabilities. The coupling of the 6D Boltzmann solver with the hydrodynamics is made recently (Nagakura et al. 2014) and numerical studies to explore the dynamical outcome for explosions are currently underway.

## Acknowledgments

We are grateful to K. Kotake, H. Suzuki for the collaborations on supernova simulations. K. S. thanks to H. Nagakura, W. Iwakami, K. Nakazato, S. Furusawa, Y. Sekiguchi, K. Kiuchi and N. Ohnishi for collaborative works and profitable discussions. K. S. expresses his thanks to T.-H. Janka, C. Ott and A. Mezzacappa for valuable comments on the numerical methods of neutrino transfer in 2D and 3D. We thank A. Imakura and T. Sakurai for the project of computational science for sparse matrix solvers and the supporting team of HITACHI for tuning the numerical code on SR16000.

The numerical computations in this work were mainly performed on the supercomputers at High Energy Accelerator Research Organization (KEK) under the support of its Large-scale Simulation Program (Nos.12/13-05, 13/14-10, 14/15-17). K. S. acknowledges also the extensive usage of the supercomputing resources at Yukawa Institute for Theoretical Physics (YITP) in Kyoto University, The University of Tokyo, K-computer and Research Center for Nuclear Physics (RCNP) in Osaka University. This research is supported by the computational resources of the K computer provided by the RIKEN Advanced Institute for Computational Science through the HPCI System Research project (Project ID:hp130025, hp140211). Large-scale storage of numerical data is supported by the JLDG constructed over the SINET4 of NII.

This work is partially supported by the Grant-in-Aid for Scientific Research on Innovative Areas (Nos. 20105004, 20105005, 24103006) and the Grant-in-Aid for the Scientific Research (Nos. 19104006, 21540281, 22540296, 24244036, 26870823) from the Ministry of Education, Culture, Sports, Science and Technology (MEXT) in Japan.

This numerical study on core-collapse supernovae using the supercomputer facilities is supported by the HPCI Strategic Program of MEXT, Japan.

## REFERENCES

- Abdikamalov, E., Burrows, A., Ott, C. D., Löffler, F., O’Connor, E., Dolence, J. C., & Schnetter, E. 2012, *ApJ*, 755, 111
- Bethe, H. A. 1990, *Rev. Mod. Phys.*, 62, 801
- Bethe, H. A., & Wilson, J. R. 1985, *ApJ*, 295, 14
- Blondin, J. M., & Mezzacappa, A. 2007, *Nature*, 445, 58
- Brandt, T. D., Burrows, A., Ott, C. D., & Livne, E. 2011, *ApJ*, 728, 8
- Bruenn, S. W. 1985, *ApJS*, 58, 771
- Bruenn, S. W., et al. 2013, *ApJ*, 767, L6
- . 2014, *ArXiv:1409.5779*
- Buras, R., Rampp, M., Janka, H., & Kifonidis, K. 2006, *A&A*, 447, 1049
- Burrows, A. 2013, *Reviews of Modern Physics*, 85, 245
- Burrows, A., Livne, E., Dessart, L., Ott, C. D., & Murphy, J. 2006, *ApJ*, 640, 878
- Cardall, C. Y., Endeve, E., & Mezzacappa, A. 2013, *Phys. Rev. D*, 88, 023011
- Dolence, J. C., Burrows, A., & Zhang, W. 2014, *arXiv:1403.6115*
- Hanke, F., Marek, A., Müller, B., & Janka, H.-T. 2012, *ApJ*, 755, 138
- Hanke, F., Müller, B., Wongwathanarat, A., Marek, A., & Janka, H.-T. 2013, *ApJ*, 770, 66
- Hayes, J. C., Norman, M. L., Fiedler, R. A., Bordner, J. O., Li, P. S., Clark, S. E.,  
ud-Doula, A., & Mac Low, M.-M. 2006, *ApJS*, 165, 188

- Hirata, K., et al. 1987, *Phys. Rev. Lett.*, 58, 1490
- Horiuchi, S., Nakamura, K., Takiwaki, T., Kotake, K., & Tanaka, M. 2014, *ArXiv:1409.0006*
- Iliev, I. T., et al. 2006, *MNRAS*, 371, 1057
- Iwakami, W., Kotake, K., Ohnishi, N., Yamada, S., & Sawada, K. 2008, *ApJ*, 678, 1207
- Janka, H., & Müller, E. 1996, *A&A*, 306, 167
- Janka, H.-T. 1992, *A&A*, 256, 452
- Janka, H.-T., Hanke, F., Hüdepohl, L., Marek, A., Müller, B., & Obergaulinger, M. 2012, *Progress of Theoretical and Experimental Physics*, 2012, 010000
- Janka, H.-T., Langanke, K., Marek, A., Martínez-Pinedo, G., & Muller, B. 2007, *Phys. Rep.*, 442, 38
- Kotake, K., Sato, K., & Takahashi, K. 2006, *Rep. Prog. Phys.*, 69, 971
- Kotake, K., Sumiyoshi, K., Yamada, S., Takiwaki, T., Kuroda, T., Suwa, Y., & Nagakura, H. 2012, *Progress of Theoretical and Experimental Physics*, 2012, 010000
- Lattimer, J. M., & Swesty, F. D. 1991, *Nucl. Phys.*, A535, 331
- Lentz, E. J., Mezzacappa, A., Bronson Messer, O. E., Hix, W. R., & Bruenn, S. W. 2012a, *ApJ*, 760, 94
- Lentz, E. J., Mezzacappa, A., Bronson Messer, O. E., Liebendörfer, M., Hix, W. R., & Bruenn, S. W. 2012b, *ApJ*, 747, 73
- Liebendörfer, M., Messer, O. E. B., Mezzacappa, A., Bruenn, S. W., Cardall, C. Y., & Thielemann, F.-K. 2004, *ApJS*, 150, 263
- Liebendörfer, M., Rampp, M., Janka, H., & Mezzacappa, A. 2005, *ApJ*, 620, 840

- Liebendörfer, M., Whitehouse, S. C., & Fischer, T. 2009, *ApJ*, 698, 1174
- Livne, E., Burrows, A., Walder, R., Lichtenstadt, I., & Thompson, T. A. 2004, *ApJ*, 609, 277
- Messer, O. E. B., Mezzacappa, A., Bruenn, S. W., & Guidry, M. W. 1998, *ApJ*, 507, 353
- Mezzacappa, A., et al. 2014, *ArXiv:1405.7075*
- Müller, B., Janka, H.-T., & Heger, A. 2012, *ApJ*, 761, 72
- Nagakura, H., Sumiyoshi, K., & Yamada, S. 2014, *ApJS*, 214, 16
- Nakamura, K., Takiwaki, T., Kuroda, T., & Kotake, K. 2014, *ArXiv:1406.2415*
- Nakazato, K., Sumiyoshi, K., Suzuki, H., Totani, T., Umeda, H., & Yamada, S. 2013, *ApJS*, 205, 2
- Nordhaus, J., Burrows, A., Almgren, A., & Bell, J. 2010, *ApJ*, 720, 694
- Ott, C. D., Burrows, A., Dessart, L., & Livne, E. 2008, *ApJ*, 685, 1069
- Shibata, M., Kiuchi, K., Sekiguchi, Y., & Suwa, Y. 2011, *Progress of Theoretical Physics*, 125, 1255
- Shibata, M., Nagakura, H., Sekiguchi, Y., & Yamada, S. 2014, *Phys. Rev. D*, 89, 084073
- Sumiyoshi, K., & Yamada, S. 2012, *Astrophys. J. Suppl.*, 199, 17
- Sumiyoshi, K., Yamada, S., Suzuki, H., Shen, H., Chiba, S., & Toki, H. 2005, *ApJ*, 629, 922
- Suwa, Y., Kotake, K., Takiwaki, T., Whitehouse, S. C., Liebendörfer, M., & Sato, K. 2010, *PASJ*, 62, L49+
- Suwa, Y., Yamada, S., Takiwaki, T., & Kotake, K. 2014, *ArXiv:1406.6414*

Takiwaki, T., Kotake, K., & Suwa, Y. 2012, ApJ, 749, 98

—. 2014a, in preparation

—. 2014b, ApJ, 786, 83

Tamborra, I., Hanke, F., Janka, H.-T., Müller, B., Raffelt, G. G., & Marek, A. 2014, ApJ, 792, 96

Thompson, T. A., Burrows, A., & Pinto, P. 2003, ApJ, 539, 865

Woosley, S. E., Heger, A., & Weaver, T. A. 2002, Reviews of Modern Physics, 74, 1015

Yamada, S., Janka, H.-T., & Suzuki, H. 1999, A&A, 344, 533

Table 1: Volume-integrated heating rates in the heating region are listed in the unit of [erg/s] for the 6D Boltzmann and ray-by-ray evaluations. The total amount of the heating rate,  $Q_\nu$  [erg/s], is calculated by the volume-integration of the specific heating rate,  $q_\nu$  [erg/g/s], times the mass density,  $\rho$  [g/cm<sup>3</sup>], where  $q_\nu$  is positive. (See the definition in §4.3. ) Relative differences of the ray-by-ray evaluation with respect to 6D Boltzmann evaluation are also listed.

Model	Timing	Ray-by-ray $Q_\nu$ [erg/s]	6D Boltzmann $Q_\nu$ [erg/s]	Relative difference [%]
11M	100 ms	$6.84 \times 10^{51}$	$6.93 \times 10^{51}$	-1.4
11M	150 ms	$4.53 \times 10^{51}$	$4.61 \times 10^{51}$	-1.7
11M	200 ms	$2.65 \times 10^{51}$	$2.68 \times 10^{51}$	-1.1
27M	150 ms	$1.25 \times 10^{52}$	$1.26 \times 10^{52}$	-0.8
27M	200 ms	$1.16 \times 10^{52}$	$1.16 \times 10^{52}$	-0.3

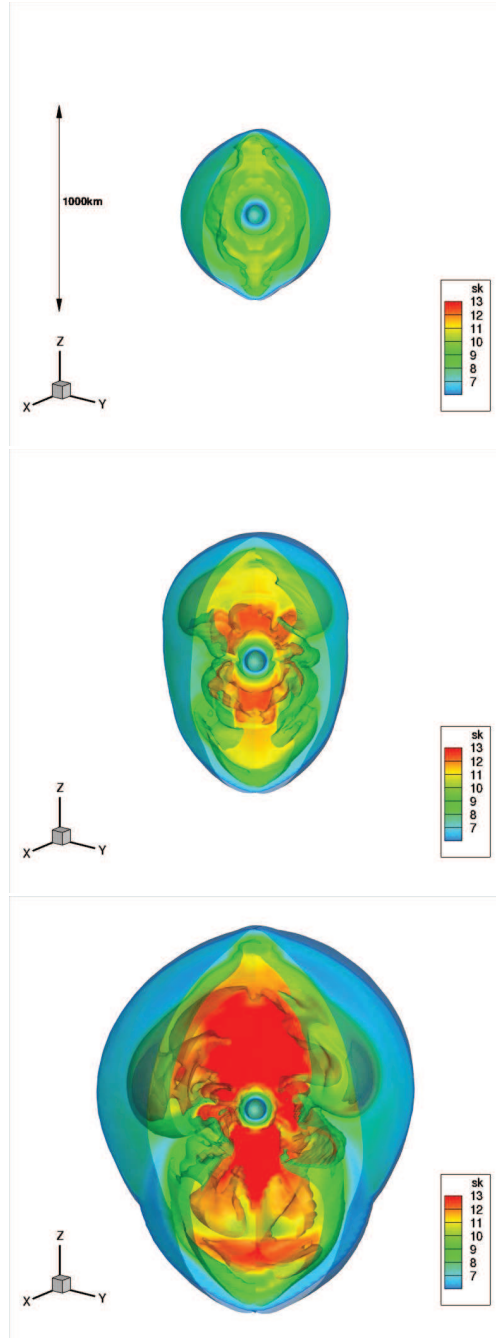


Fig. 1.— Profiles of the 3D supernova core from the simulation of  $11.2M_{\odot}$  star (Takiwaki et al. 2012). Iso-surfaces of the entropy per baryon in the unit of the Boltzmann constant,  $k_B$ , are shown for the snapshots at 100, 150 and 200 ms after the bounce in the top, middle and bottom panels, respectively.

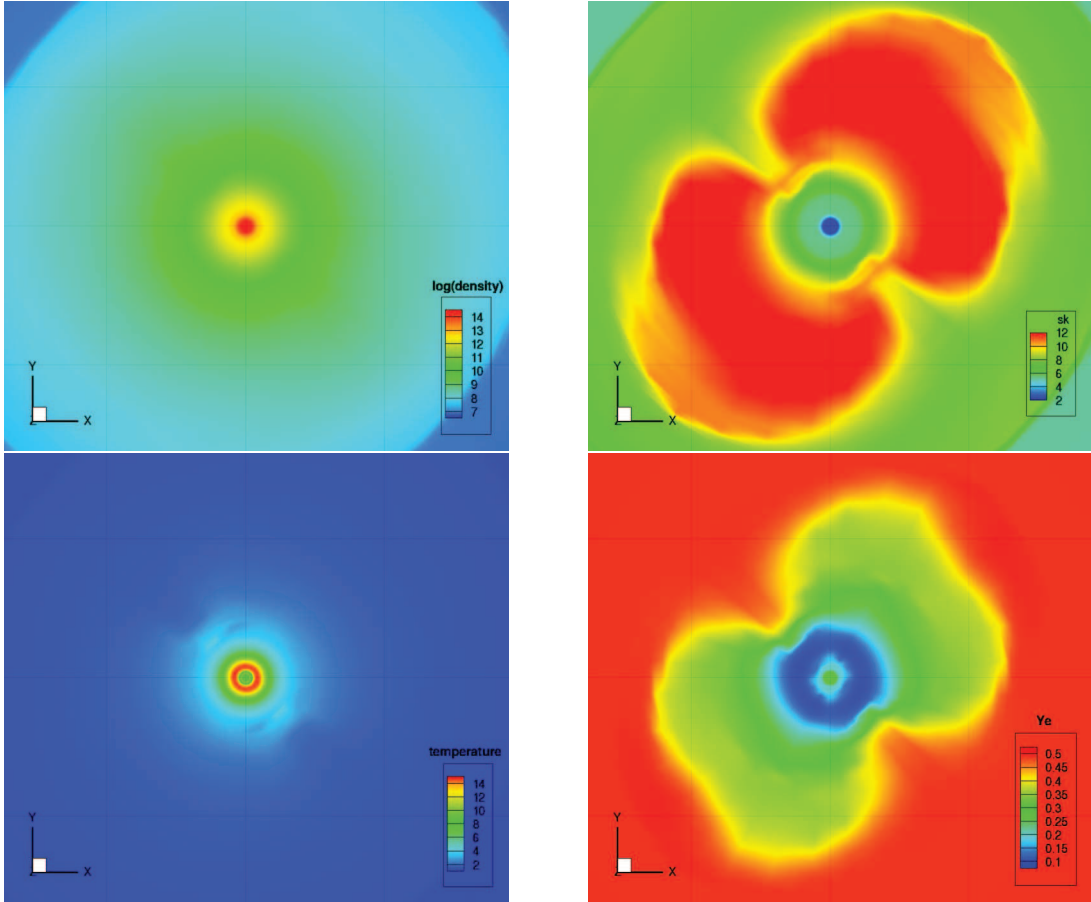


Fig. 2.— Color maps of the 3D supernova core (11M) on the xy-plane ( $z=0$ ) are shown at 150 ms after the bounce. Density [ $\text{g}/\text{cm}^3$ ], entropy per baryon [ $k_B$ ], temperature [MeV] and electron fraction are displayed in the left-top, right-top, left-bottom and right-bottom panels, respectively. Grid lines with 200 km spacing are shown in the background.

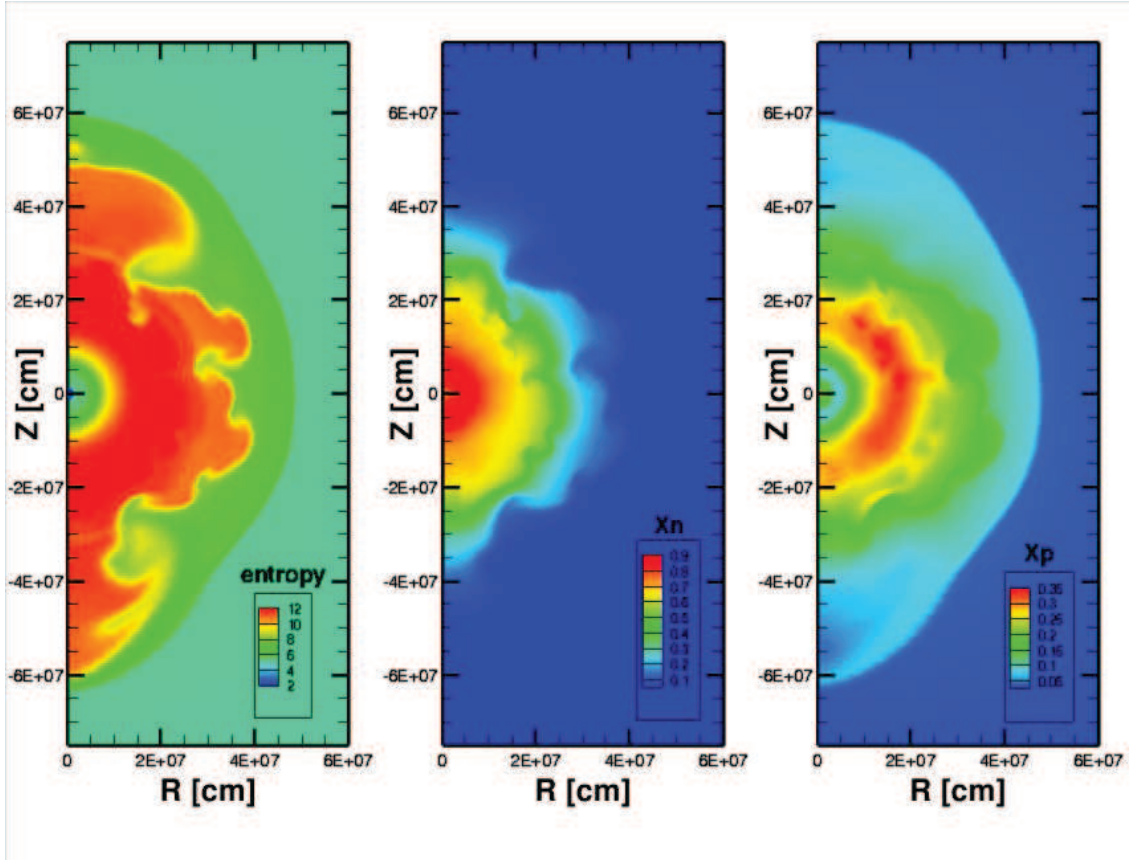


Fig. 3.— Color maps of the 3D supernova core (11M) on the meridian slice at  $\phi=51^\circ$  are shown at 150 ms after the bounce. Entropy per baryon  $[k_B]$  and mass fractions of free neutrons and protons are displayed in the left, middle and right panels, respectively.

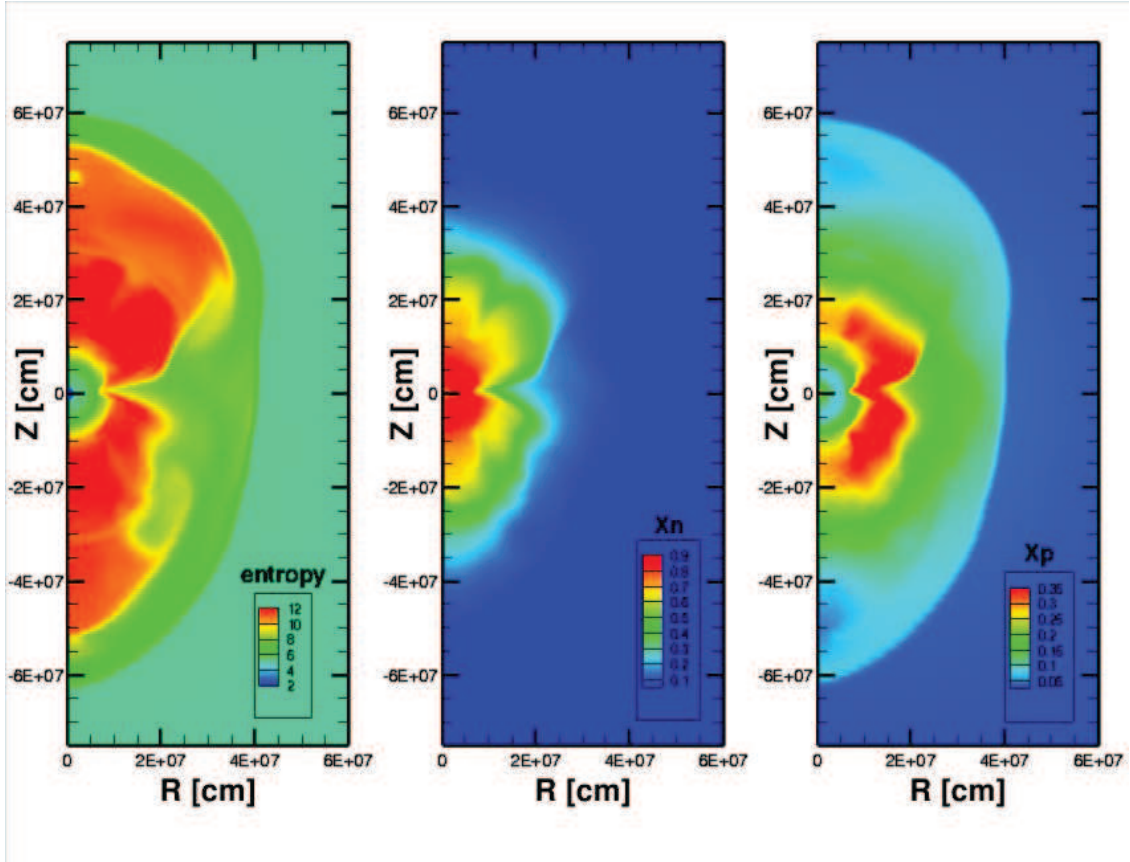


Fig. 4.— Same as Figure 3, but on the meridian slice at  $\phi=141^\circ$ .

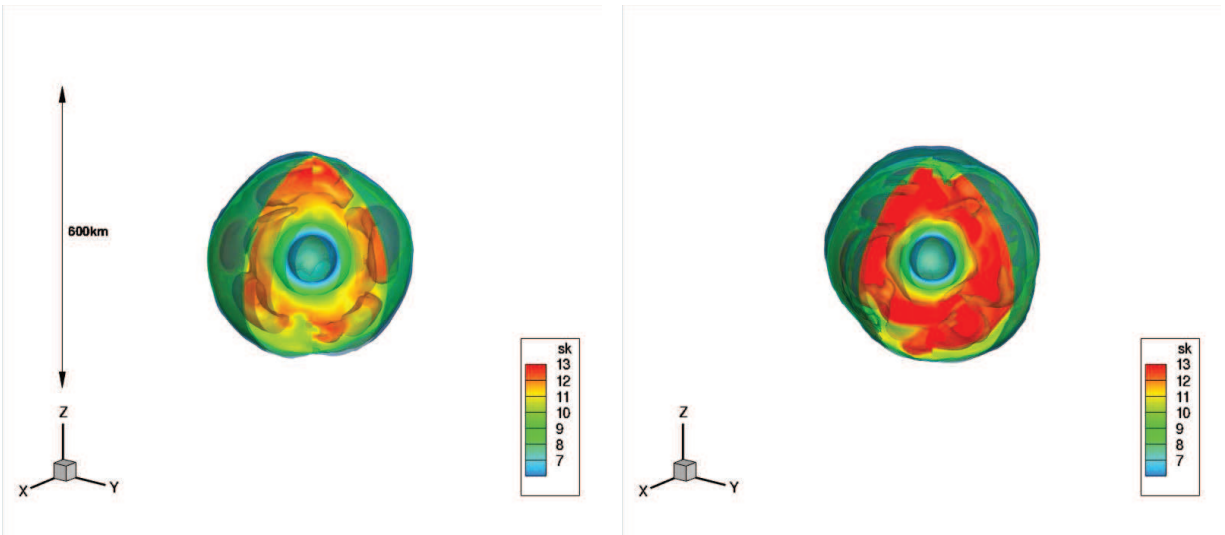


Fig. 5.— Profiles of the 3D supernova core from the simulation of  $27.0M_{\odot}$  star (Horiuchi et al. 2014; Takiwaki et al. 2014a). Iso-surfaces of the entropy per baryon in the unit of the Boltzmann constant,  $k_B$ , are shown for the snapshots at 150 and 200 ms after the bounce in the left and right panels, respectively.

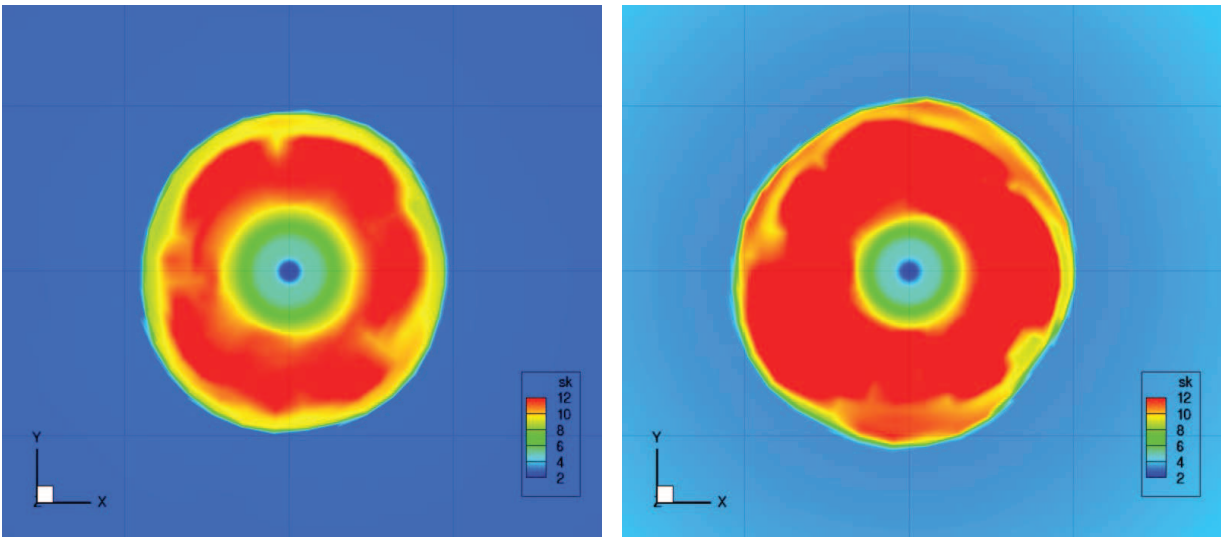


Fig. 6.— Profiles of the 3D supernova core (27M) are shown for the snapshots at 150 and 200 ms after the bounce in the left and right panels, respectively. Entropy per baryon [ $k_B$ ] is plotted by color maps on the  $xy$ -plane ( $z=0$ ). Grid lines with 200 km spacing are shown in the background.

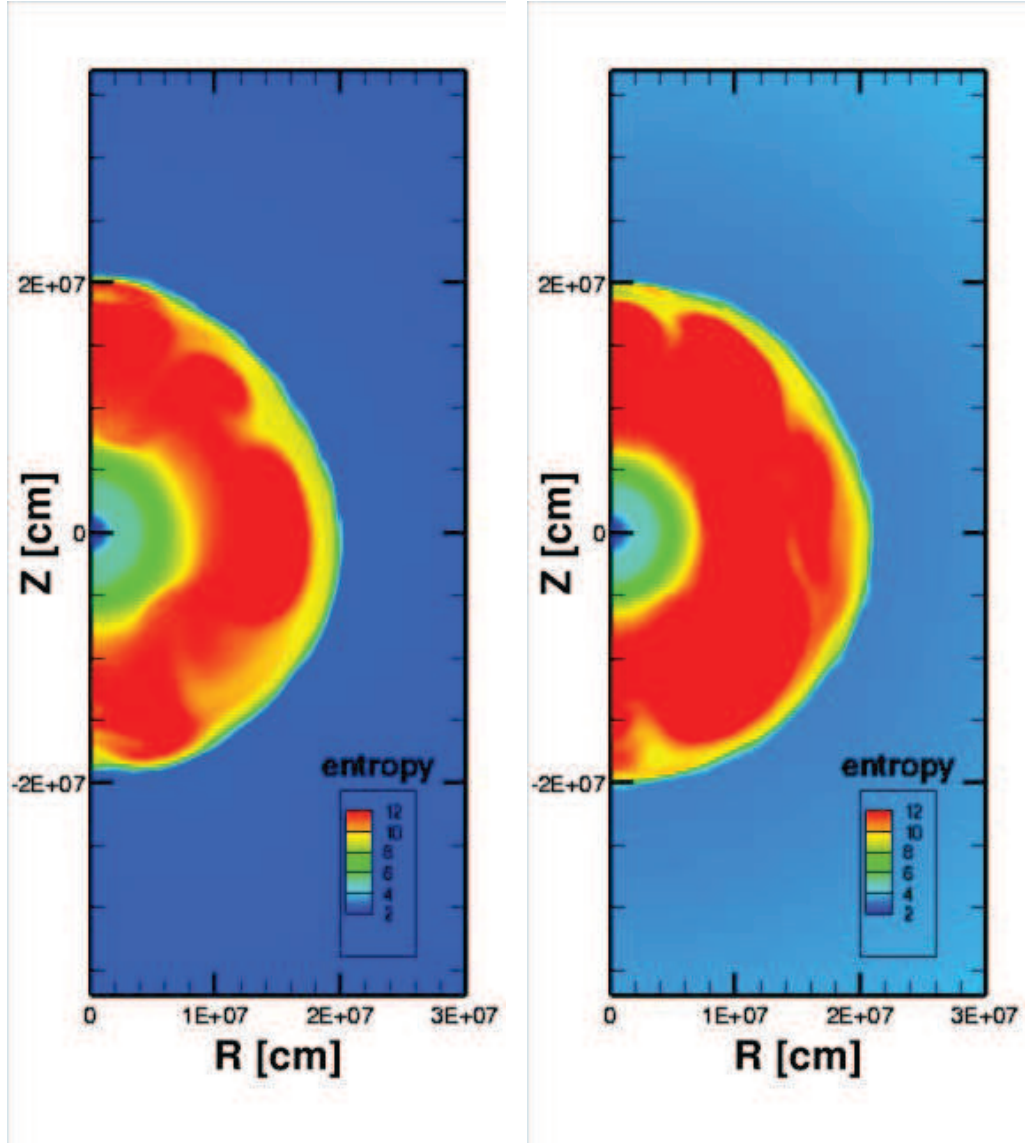


Fig. 7.— Profiles of the 3D supernova core (27M) at 150 and 200 ms after the bounce are shown on the meridian slice at  $\phi=51^\circ$  in the left and right panels, respectively. Entropy per baryon  $[k_B]$  is shown by color maps.

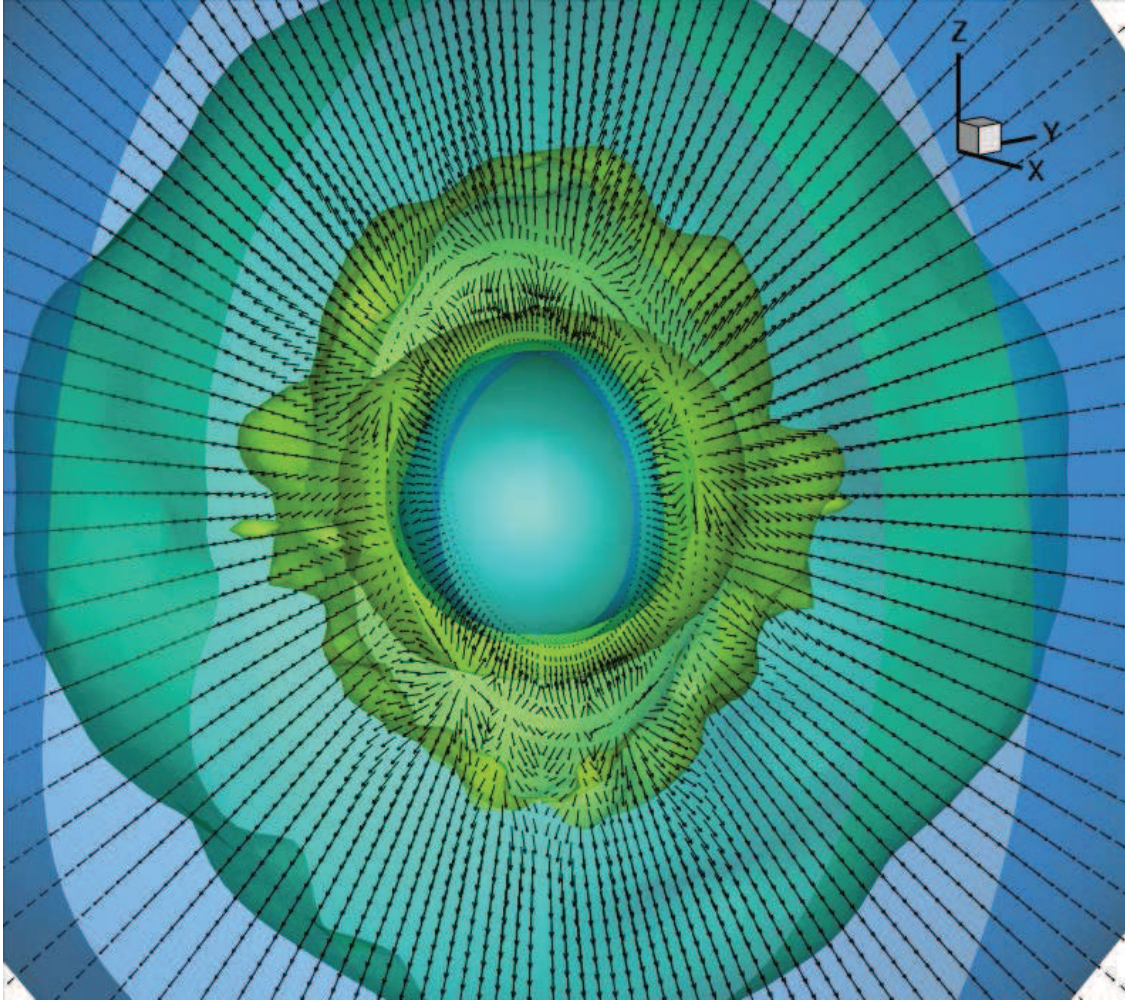


Fig. 8.— Iso-surfaces of the density of electron-type anti-neutrinos ( $\bar{\nu}_e$ ) for the 11M model at 150 ms after the bounce. Arrows represent the flux vector of neutrinos.

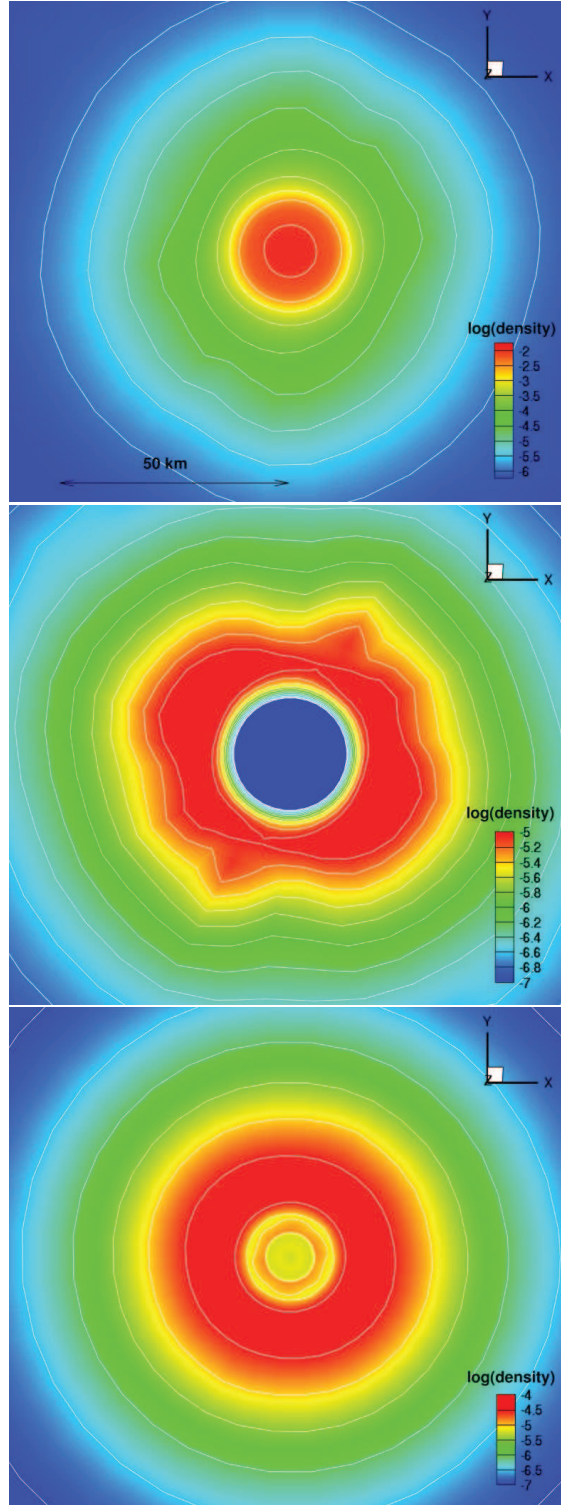


Fig. 9.— Color maps of the neutrino density in log scale in the unit of  $\text{fm}^{-3}$  for three species ( $\nu_e$ ,  $\bar{\nu}_e$  and  $\nu_\mu$ ) on the xy-plane ( $z=0$ ) are shown for the 11M model at 150 ms after the bounce in the top, middle and bottom panels, respectively.

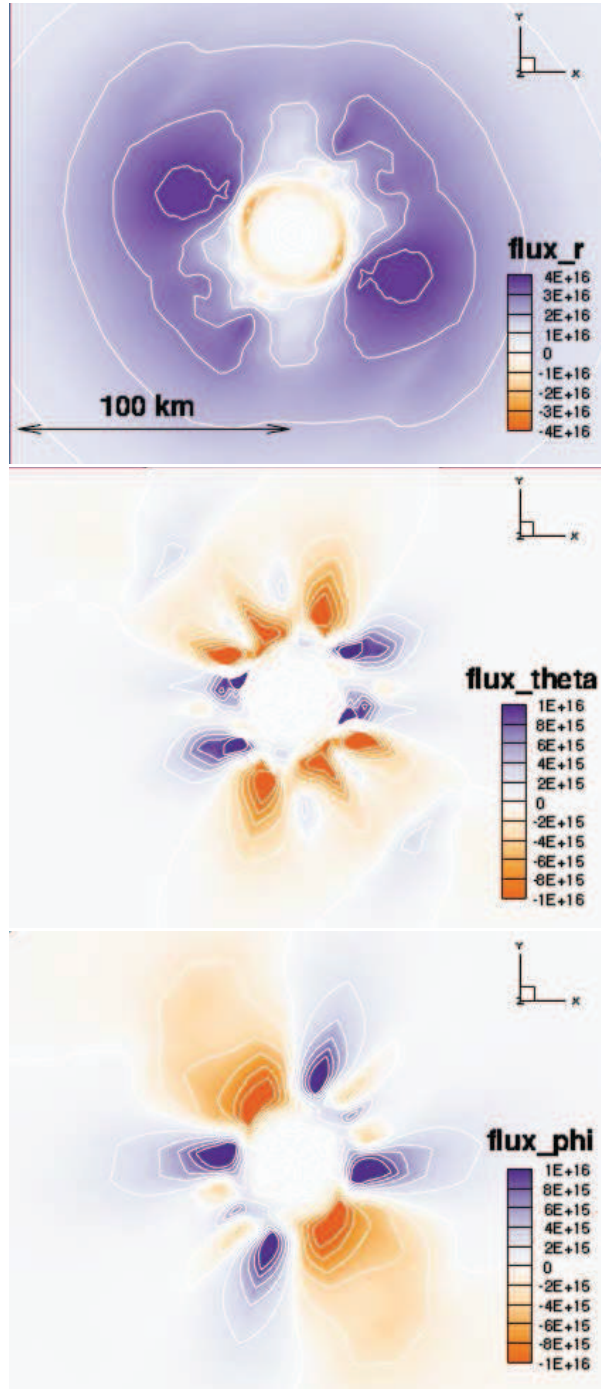


Fig. 10.— Color maps of the number flux of  $\bar{\nu}_e$  in the unit of  $\text{fm}^{-2}\text{s}^{-1}$  on the  $xy$ -plane ( $z=0$ ) are shown for the 11M model at 150 ms after the bounce. The radial, polar and azimuthal fluxes are shown in the top, middle and bottom panels, respectively.

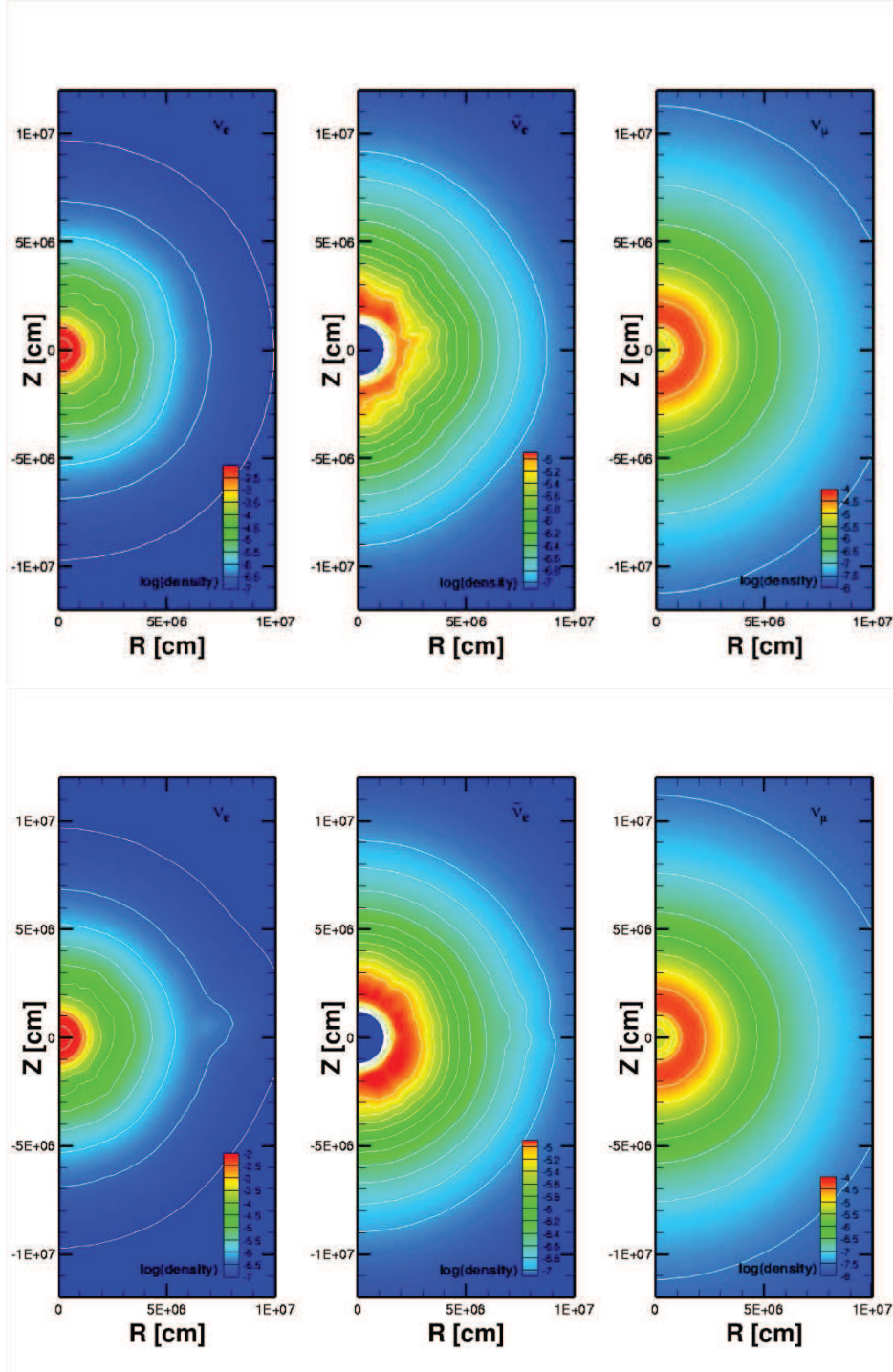


Fig. 11.— Profiles of the neutrino density on the meridian slices at  $\phi=51^\circ$  (top) and  $141^\circ$  (bottom) are shown for the 11M model at 150 ms after the bounce. The neutrino densities in log scale in the unit of  $\text{fm}^{-3}$  for three species ( $\nu_e$ ,  $\bar{\nu}_e$  and  $\nu_\mu$ ) are plotted by color maps in the left, middle and right panels, respectively.

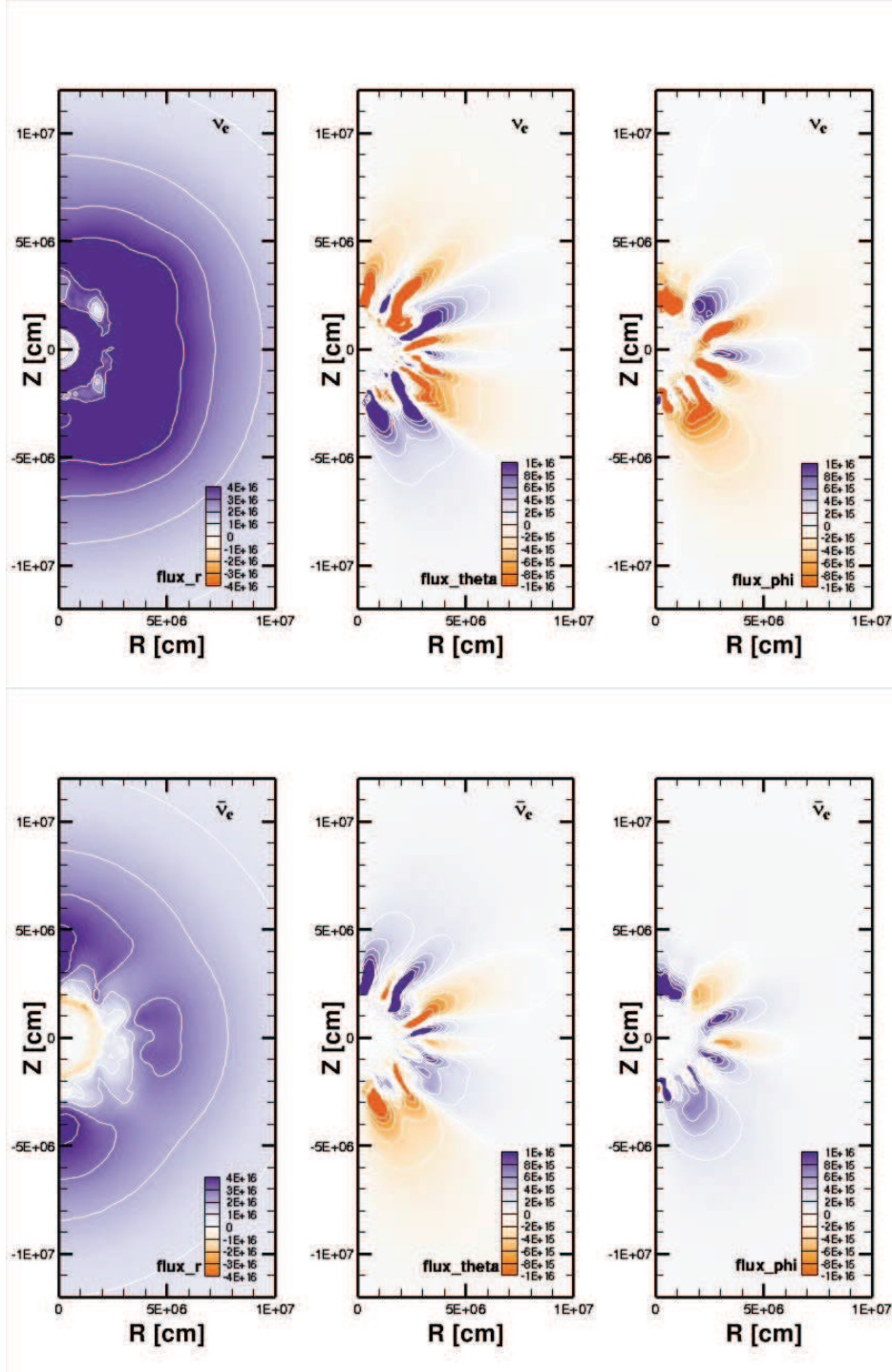


Fig. 12.— Profiles of the number flux of  $\nu_e$  (top) and  $\bar{\nu}_e$  (bottom) in the unit of  $\text{fm}^{-2}\text{s}^{-1}$  on the meridian slice at  $\phi=51^\circ$  are shown for the 11M model at 150 ms after the bounce. The radial, polar and azimuthal fluxes are plotted by color maps in the left, middle and right panels, respectively.

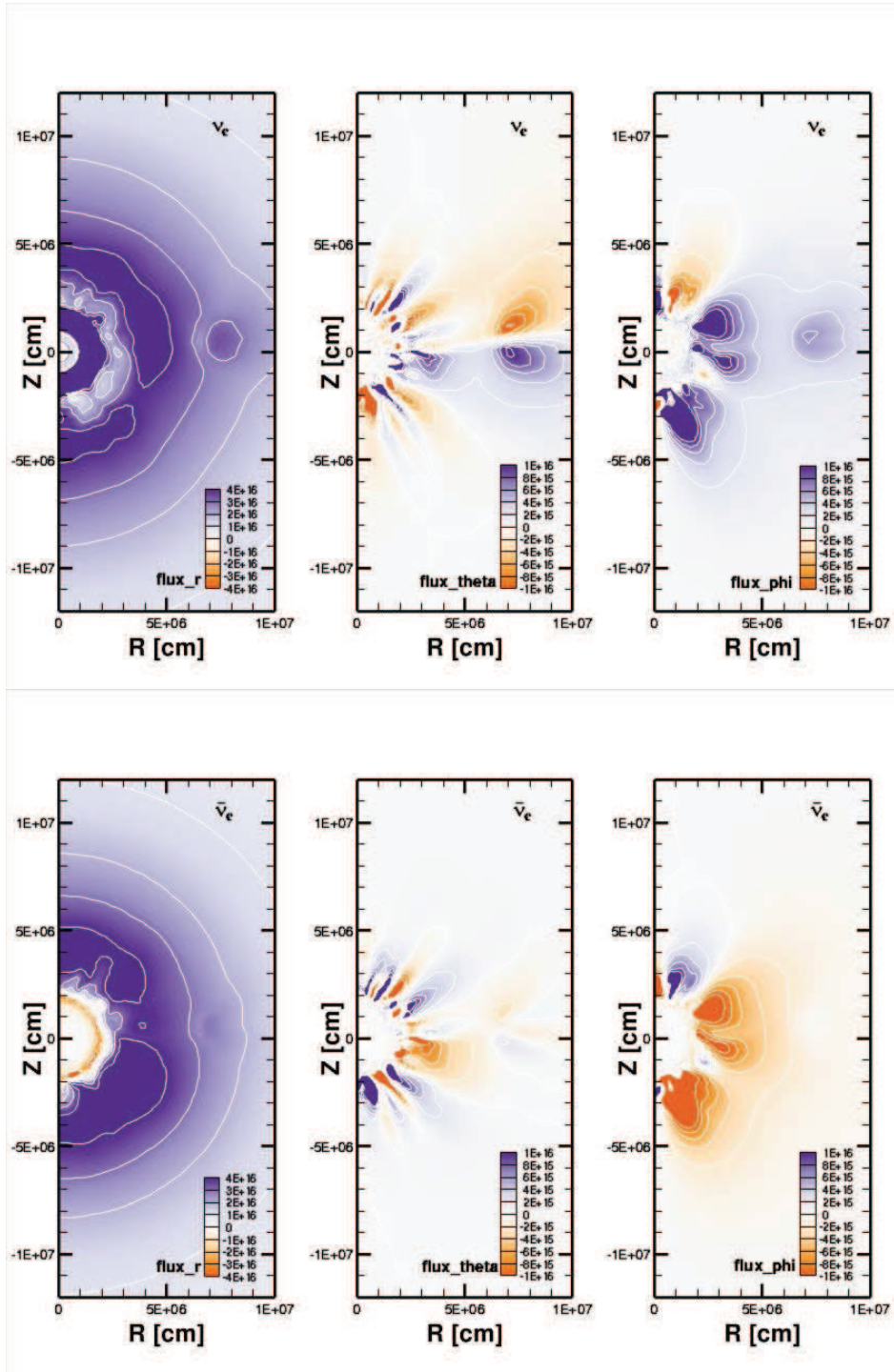


Fig. 13.— Same as Figure 12 but on the meridional slice at  $\phi=141^\circ$ .

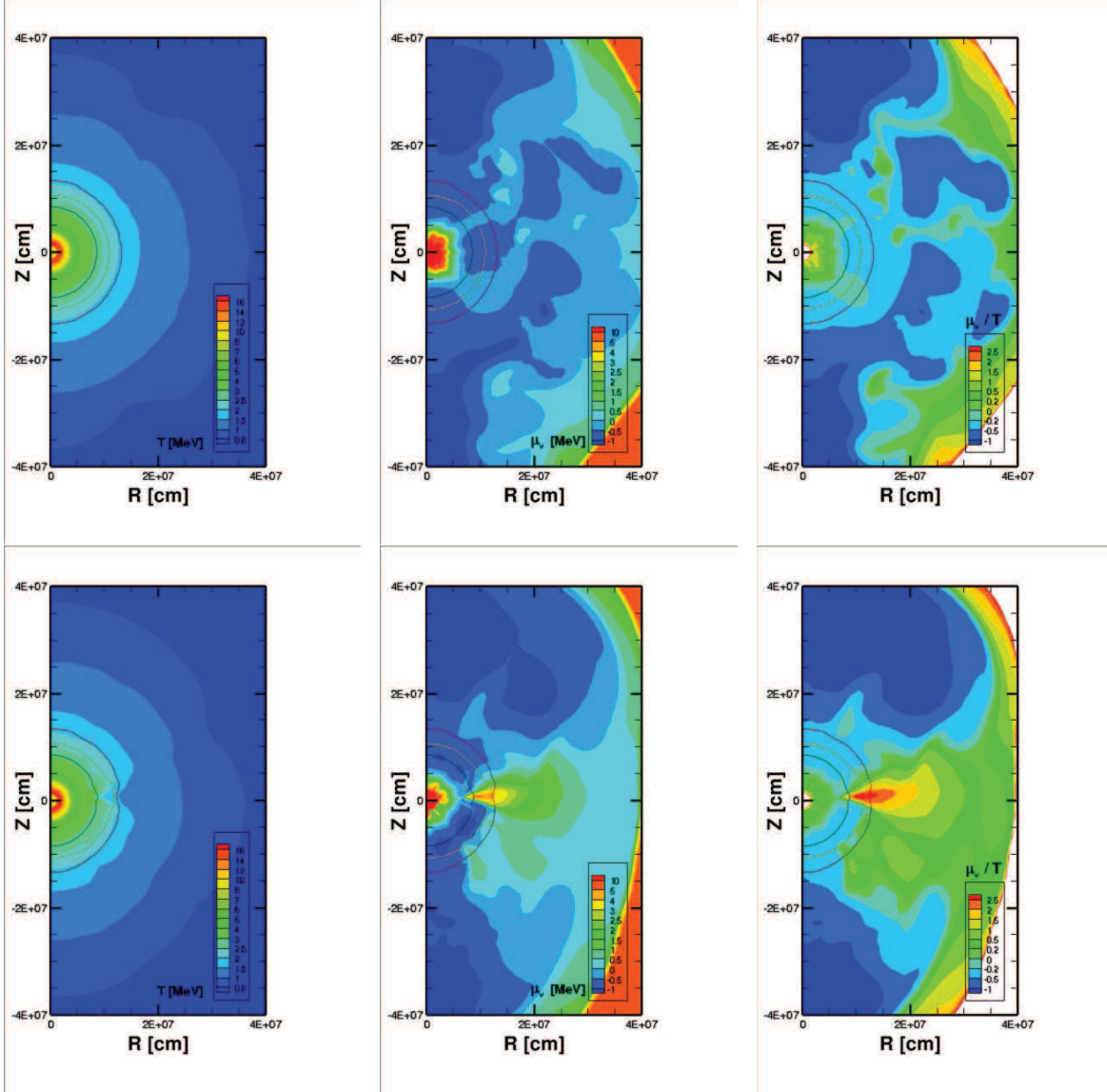


Fig. 14.— Profiles of temperature [MeV] (left), chemical potential [MeV] (center) and degeneracy of neutrinos (right) with the location of neutrino-sphere on the meridian slices at  $\phi=51^\circ$  (top) and  $141^\circ$  (bottom) are shown for the 11M model at 150 ms after the bounce. The neutrino-spheres for  $\nu_e$ ,  $\bar{\nu}_e$  and  $\nu_\mu$  are shown in the order from outside to the center.

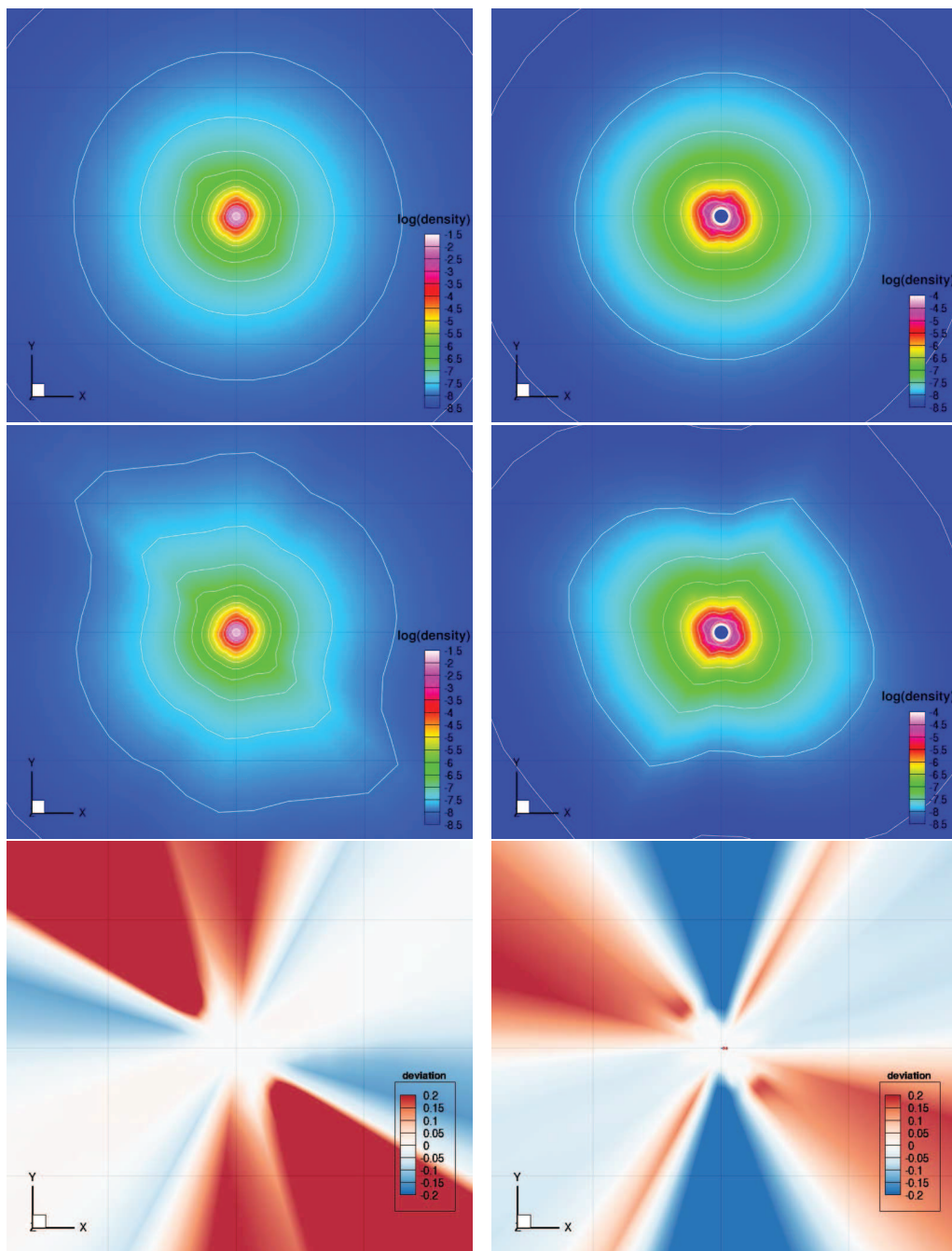


Fig. 15.— Comparison of the neutrino densities for two species ( $\nu_e$  and  $\bar{\nu}_e$ ) on the  $xy$ -plane ( $z=0$ ) is displayed by color maps in the left and right panels, respectively. The setting of the 3D supernova core (11M) at 150 ms is the same as in Fig. 9. The neutrino densities evaluated by the 6D Boltzmann solver (top) and the ray-by-ray approximation (middle) are displayed together with the relative differences between the two evaluations (bottom). Grid lines with 200 km spacing are shown in the background.

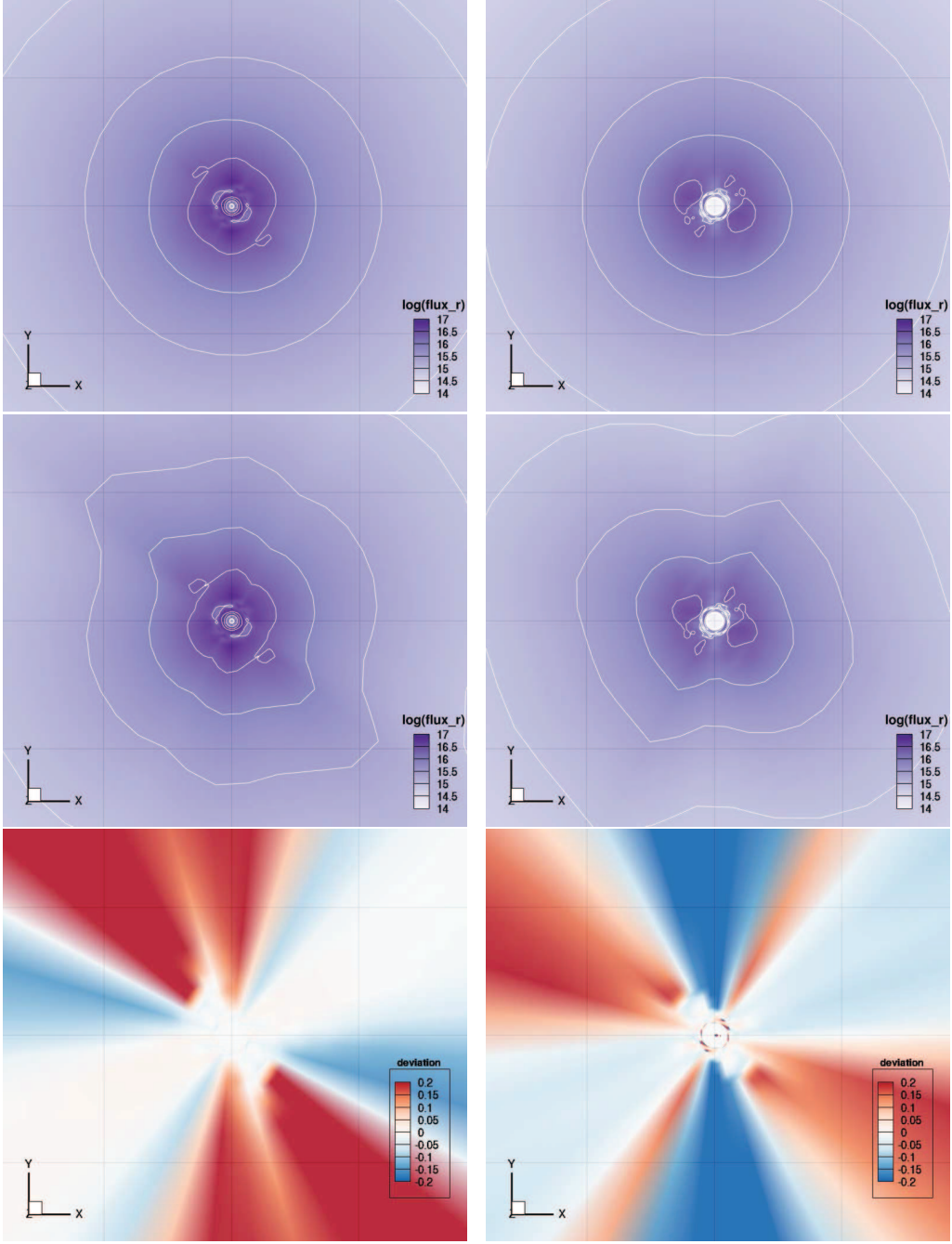


Fig. 16.— Comparison of the number fluxes in log scale in the unit of  $\text{fm}^{-2}\text{s}^{-1}$  for two species ( $\nu_e$  and  $\bar{\nu}_e$ ) on the  $xy$ -plane ( $z=0$ ) is displayed by color maps in the left and right panels, respectively. The setting of the 3D supernova core (11M) at 150 ms is the same as in Fig. 10. The radial fluxes evaluated by the 6D Boltzmann solver (top) and the ray-by-ray approximation (middle) are displayed together with the relative differences between the two evaluations (bottom). Grid lines with 200 km spacing are shown in the background.

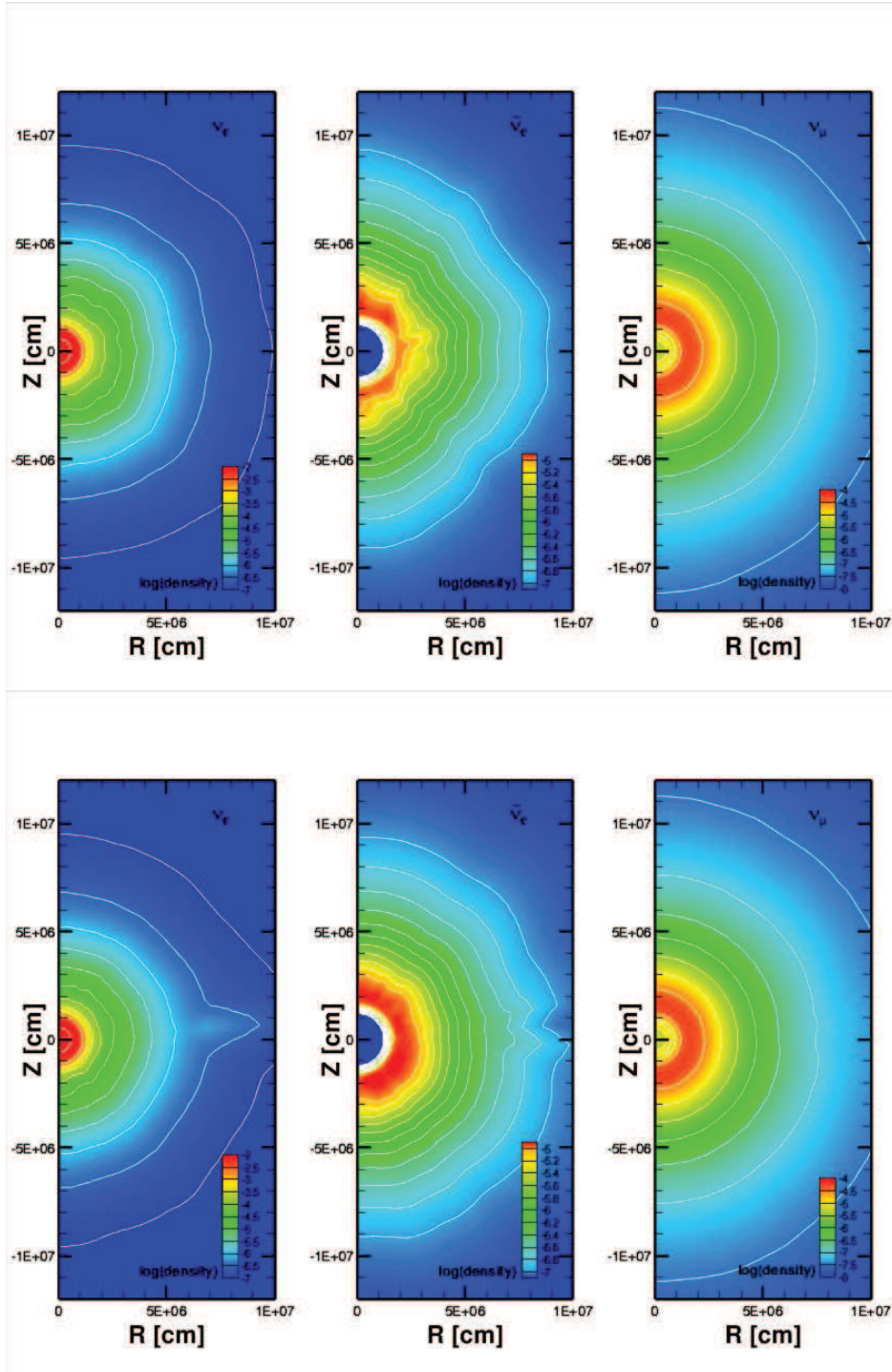


Fig. 17.— Profiles of the neutrino density evaluated by the ray-by-ray approximation for the 11M model at 150 ms. The locations of meridian slice and the notation are the same as in Fig. 11.

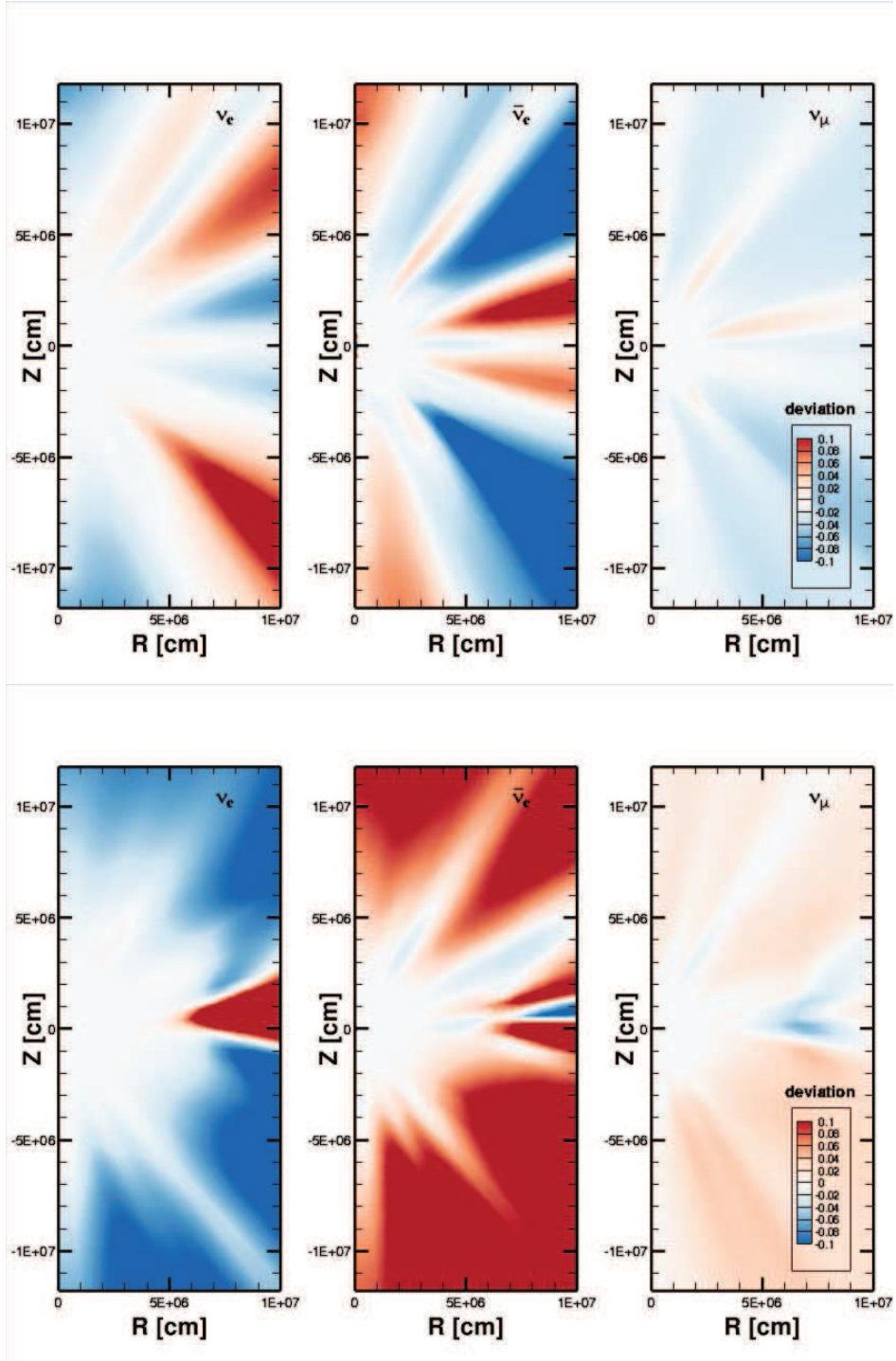


Fig. 18.— Color maps for the relative differences of the neutrino density by the ray-by-ray evaluation with respect to the 6D Boltzmann evaluation for the 11M model at 150 ms corresponding to Figs. 11 and 17.

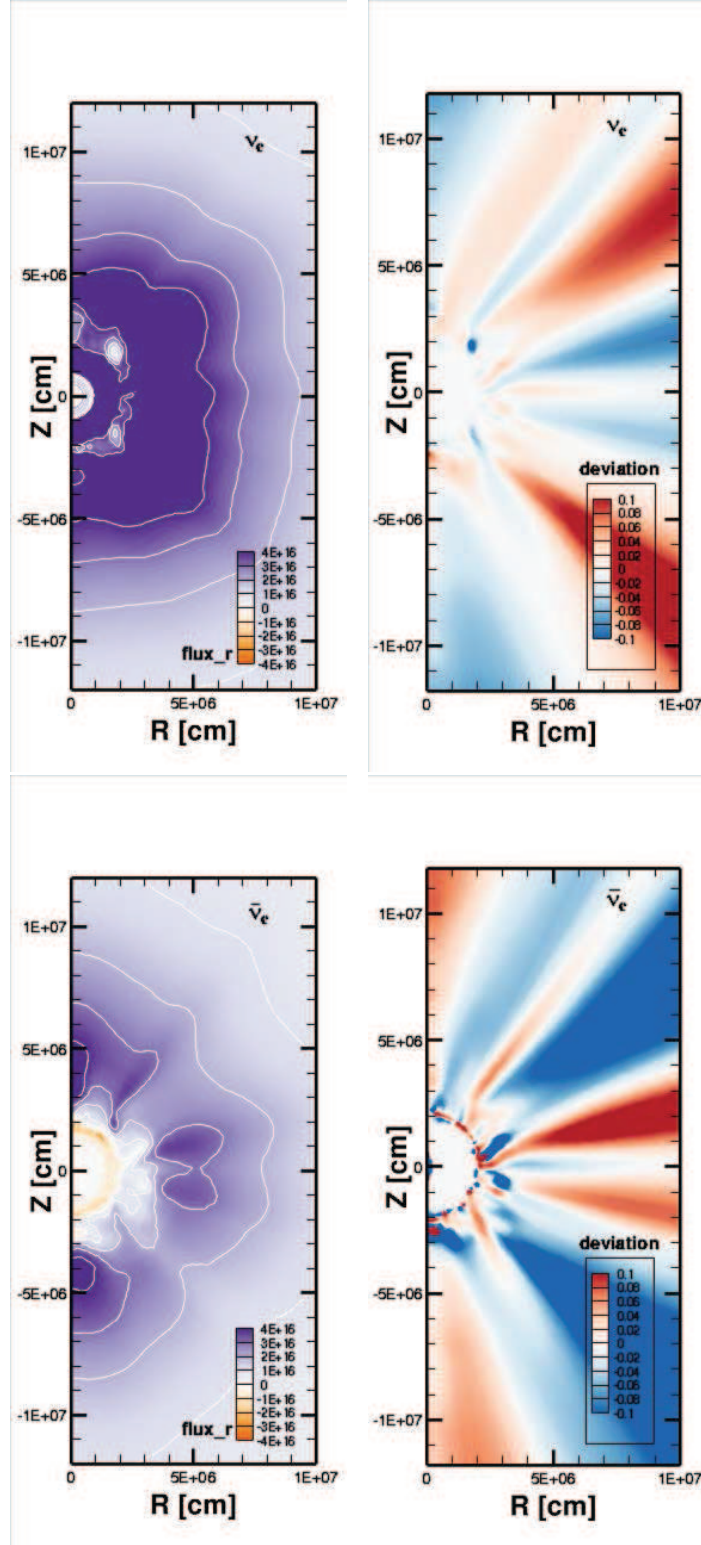


Fig. 19.— Profiles of the number flux of  $\nu_e$  (top) and  $\bar{\nu}_e$  (bottom) in the ray-by-ray approximation and its relative differences with respect to the 6D Boltzmann evaluation on the meridian slice at  $\phi=51^\circ$  are shown in the left and right panels, respectively, for the 11M model at 150 ms corresponding to Fig. 12.

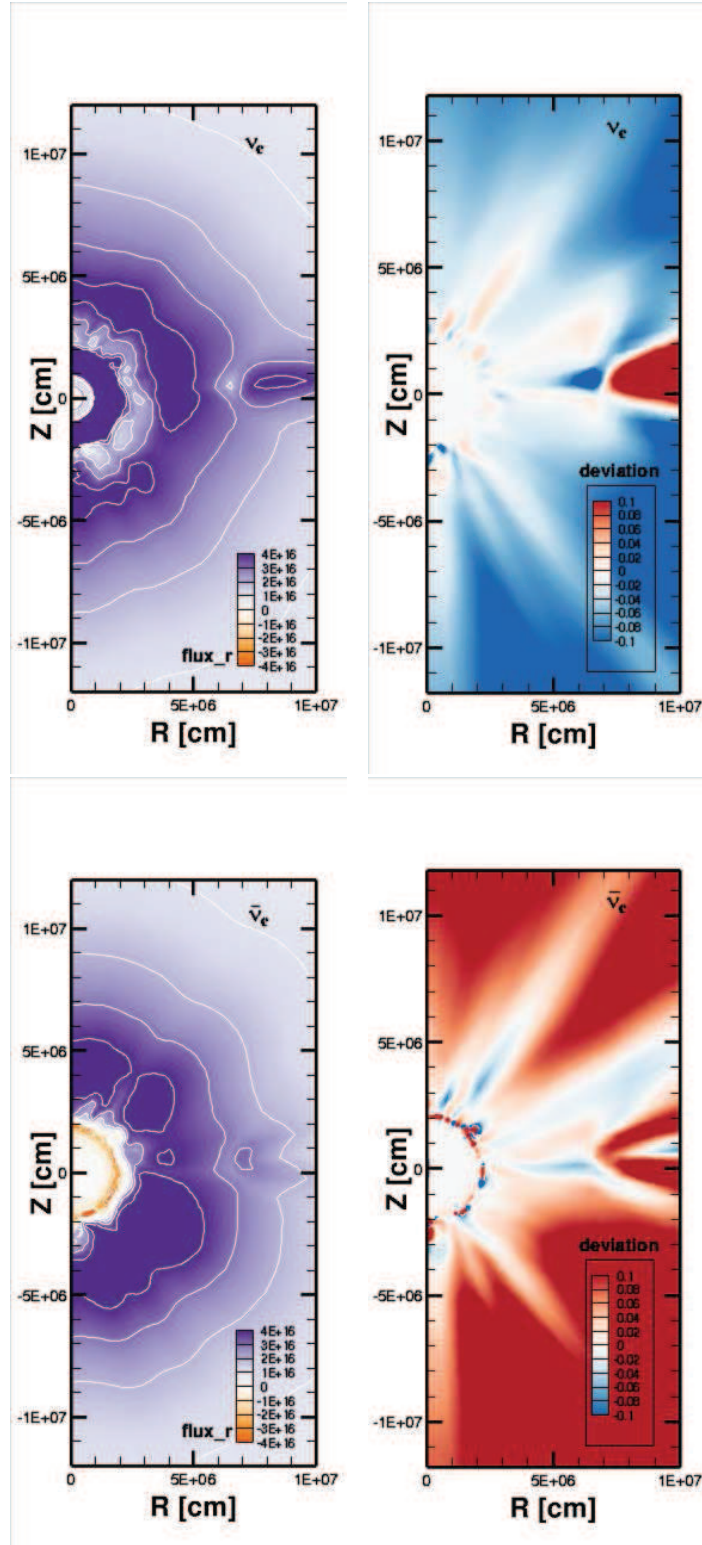


Fig. 20.— Same as Figure 19 but on the meridial slice at  $\phi=141^\circ$  corresponding to Fig. 13.

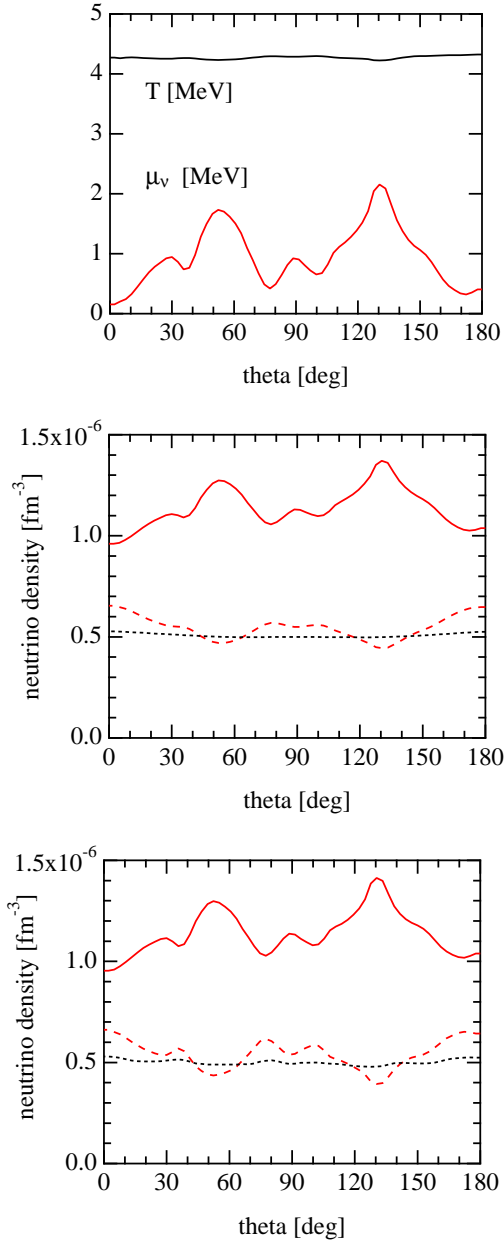


Fig. 21.— Distributions of temperature and neutrino chemical potential (top) and the neutrino densities by 6D Boltzmann (middle) and ray-by-ray evaluations (bottom) are plotted as functions of the polar angle at the radius of 54 km on the meridian slice at  $\phi=51^\circ$  for the 11M model at 150 ms. In the middle and bottom panels, red solid, red dashed and black dotted lines denote densities for  $\nu_e$ ,  $\bar{\nu}_e$  and  $\nu_\mu$ , respectively.

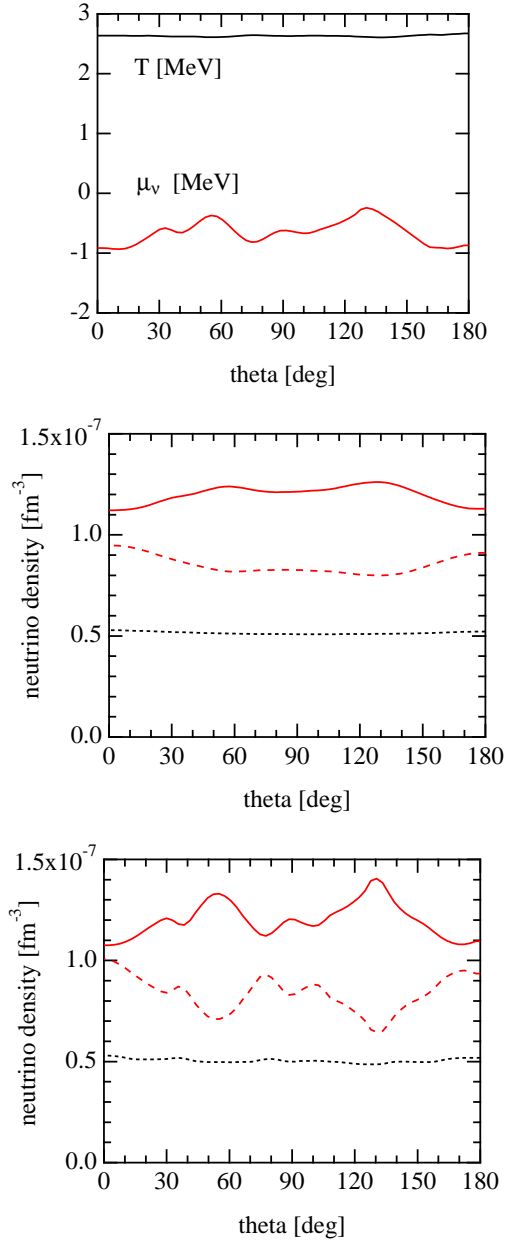


Fig. 22.— Same as Fig. 21, but at the radius of 94 km.

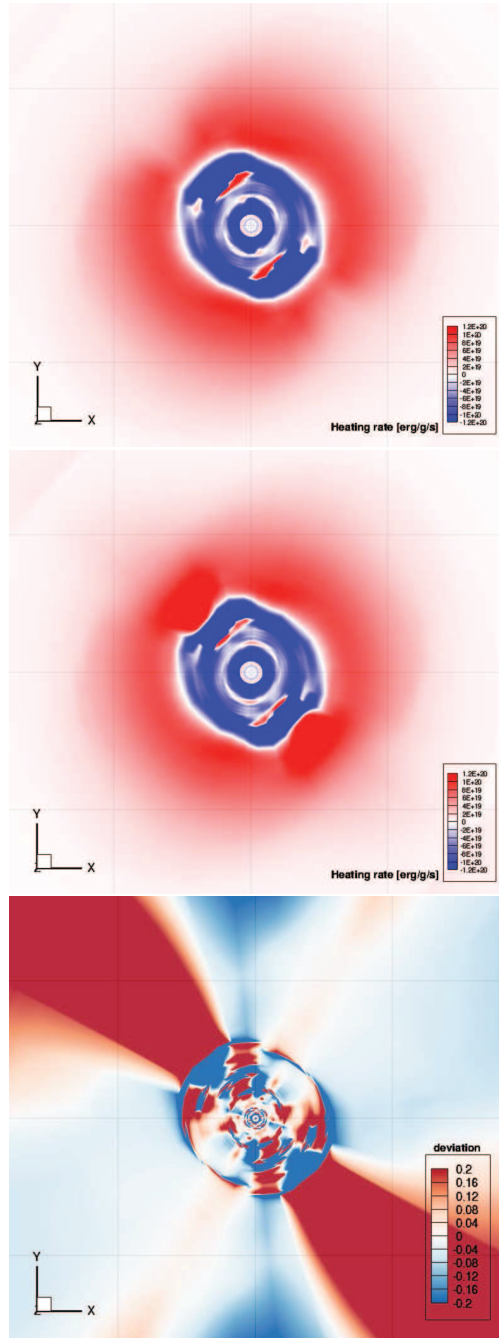


Fig. 23.— Color maps for the neutrino-heating rate on the  $xy$ -plane are shown for the 11M model at 150 ms after the bounce. The top and middle panels display the energy transfer rates via neutrinos (heating by red and cooling by blue) evaluated by the 6D Boltzmann solver and the ray-by-ray approximation, respectively. The relative difference of the ray-by-ray evaluation with respect to the 6D Boltzmann evaluation is shown in the bottom panel. Grid lines with 200 km spacing are shown in the background.

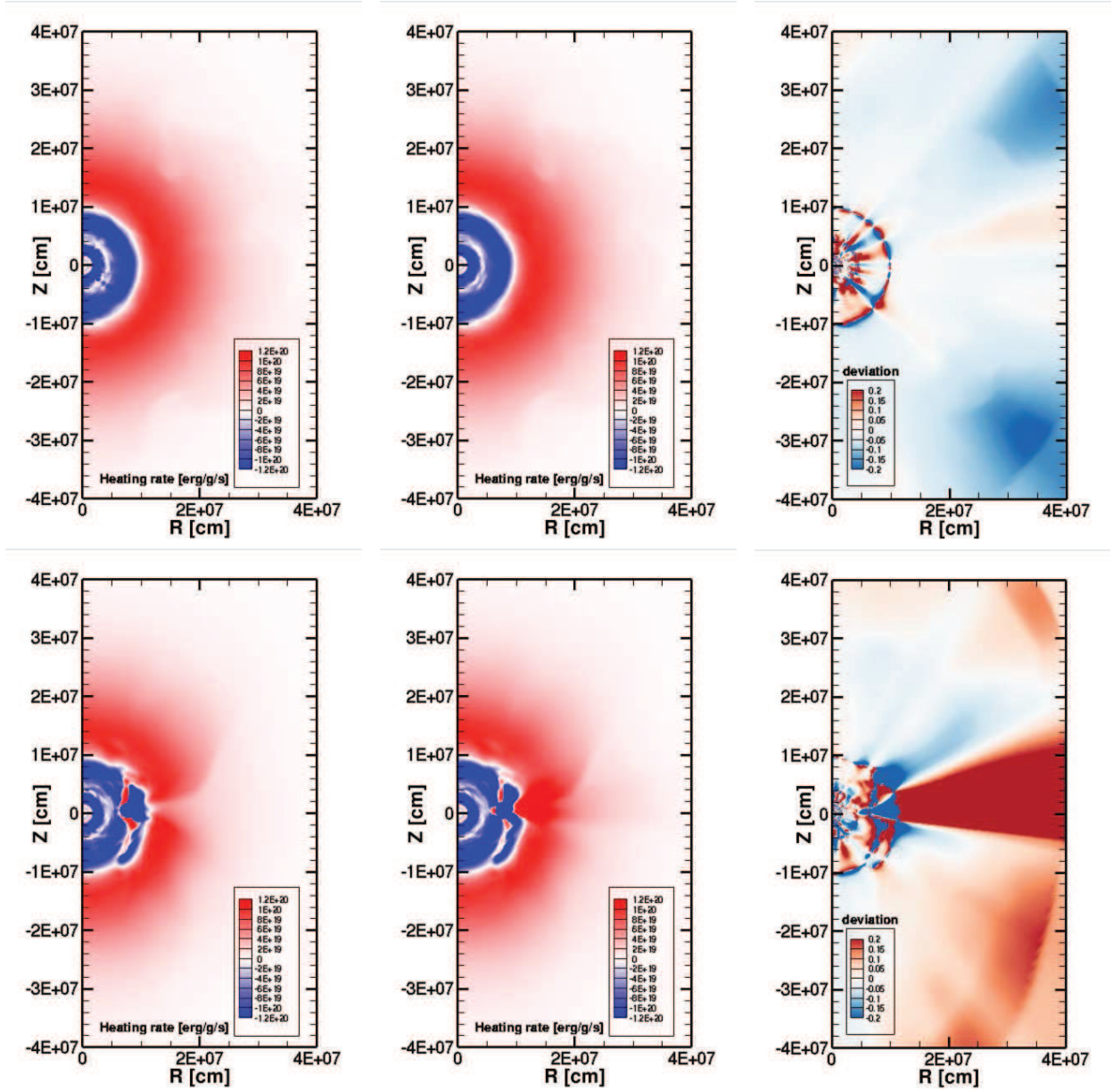


Fig. 24.— Color maps for the neutrino-heating rate on the meridian slices at  $\phi=51^\circ$  and  $141^\circ$  are shown for the 11M model at 150 ms after the bounce in the upper and lower panels, respectively. The left and middle panels display the energy transfer rates via neutrinos evaluated by the 6D Boltzmann solver and the ray-by-ray approximation, respectively. The relative difference of the ray-by-ray evaluation with respect to the 6D Boltzmann evaluation is shown in the right panel.

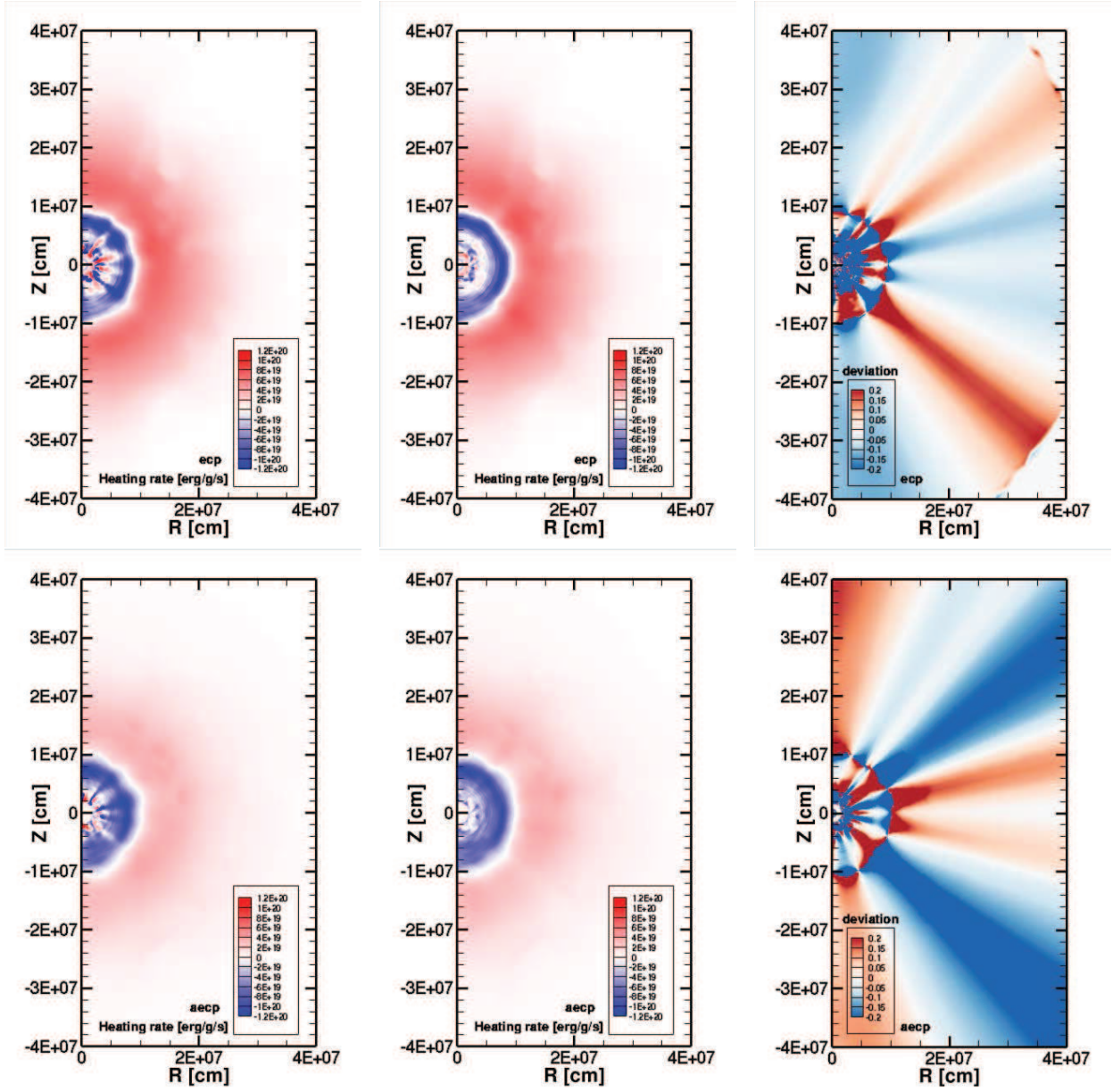


Fig. 25.— Color maps for the heating rate via  $\nu_e$  and  $\bar{\nu}_e$  absorptions on nucleons on the meridian slice at  $\phi=51^\circ$  are shown for the 11M model at 150 ms in the upper and lower panels, respectively. The left and middle panels display the 6D Boltzmann and ray-by-ray evaluations together with the relative difference of the ray-by-ray evaluation in the right panel.

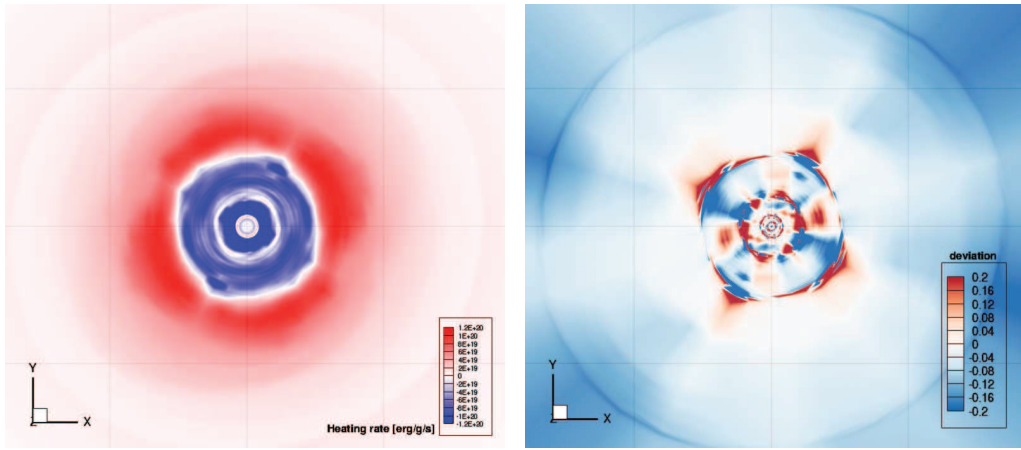


Fig. 26.— Color maps of the heating rate obtained by the 6D Boltzmann solver for the 11M model at 100 ms after the bounce are shown in the left panel. The relative difference of the ray-by-ray evaluation is shown in the right panel. Grid lines with 200 km spacing are shown in the background.

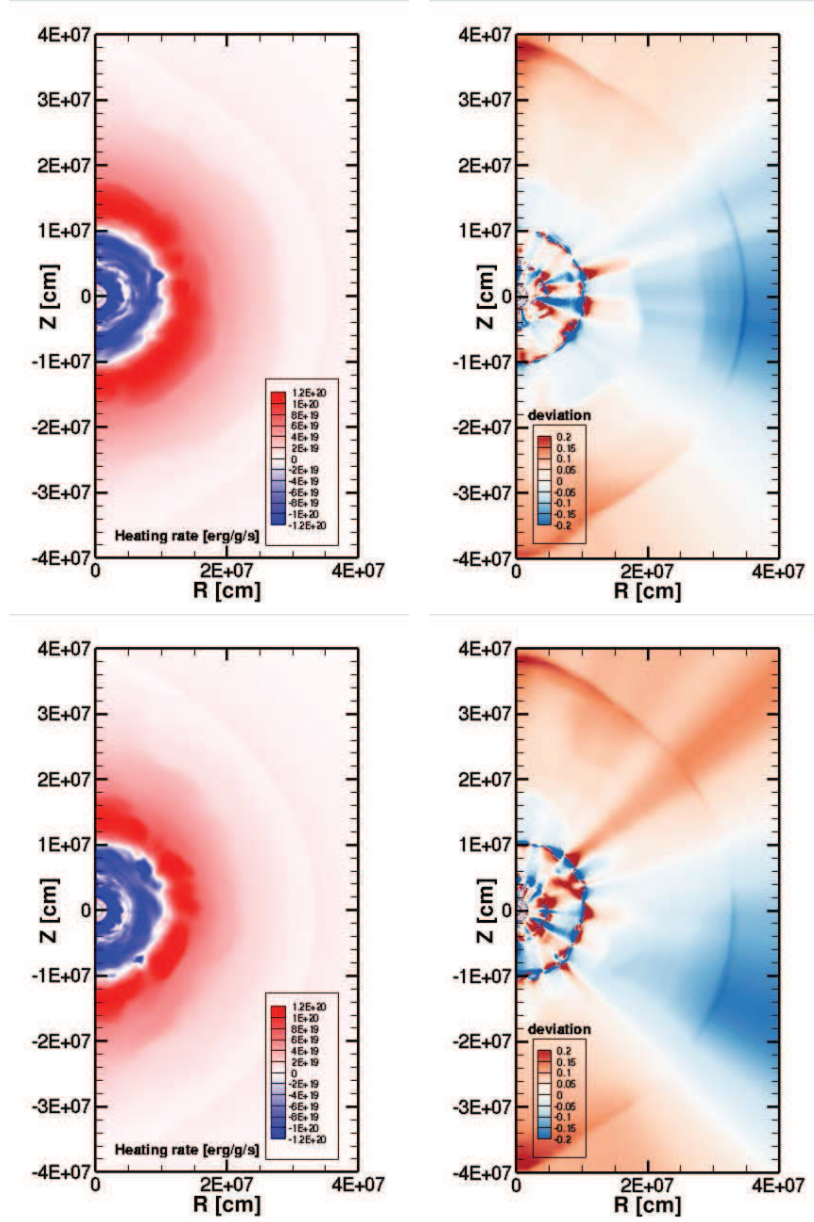


Fig. 27.— Color maps of the heating rate by the 6D Boltzmann evaluation are shown in the left panels for the 11M model at 100 ms after the bounce. The corresponding profiles for the relative difference of the ray-by-ray evaluation are shown in the right panels. The top and bottom panels show the profiles on the meridian slices at  $\phi=51^\circ$  and  $141^\circ$ , respectively.

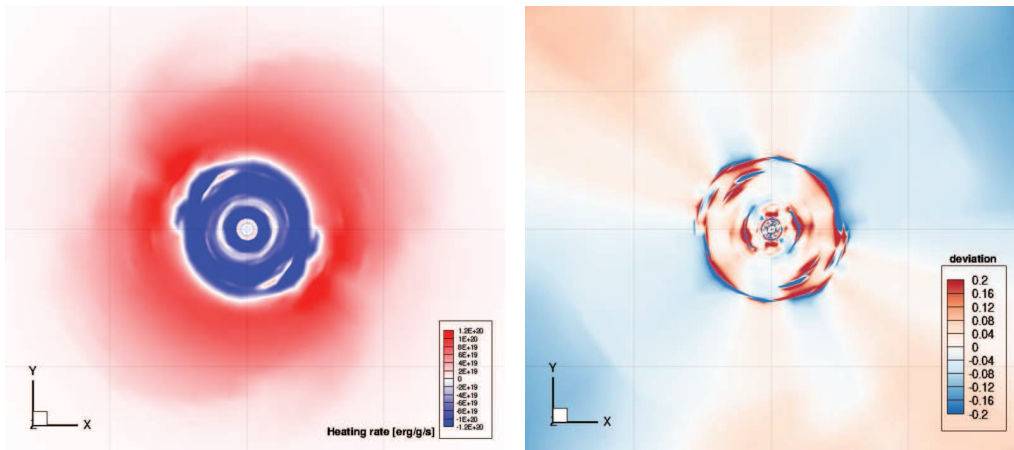


Fig. 28.— Same as Fig. 26 but for the 11M model at 200 ms after the bounce.

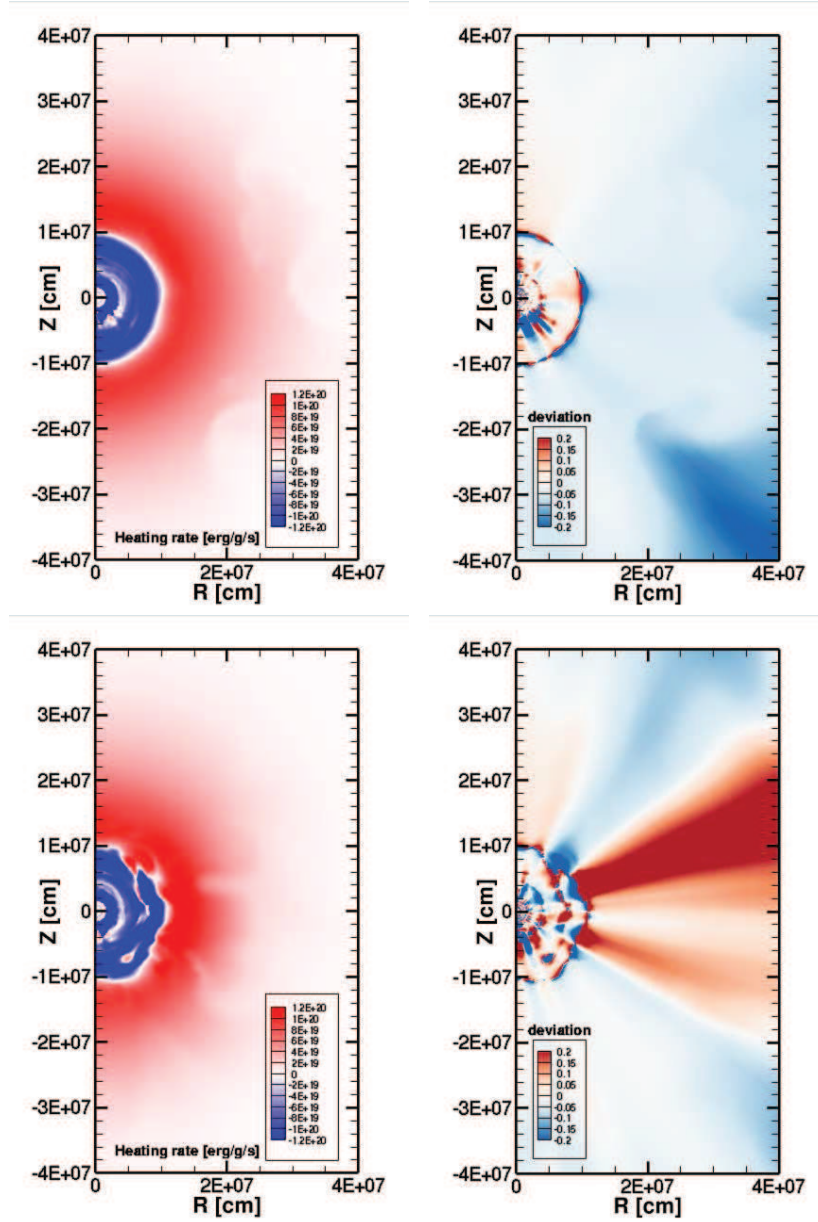


Fig. 29.— Same as Fig. 27 but for the 11M model at 200 ms after the bounce.

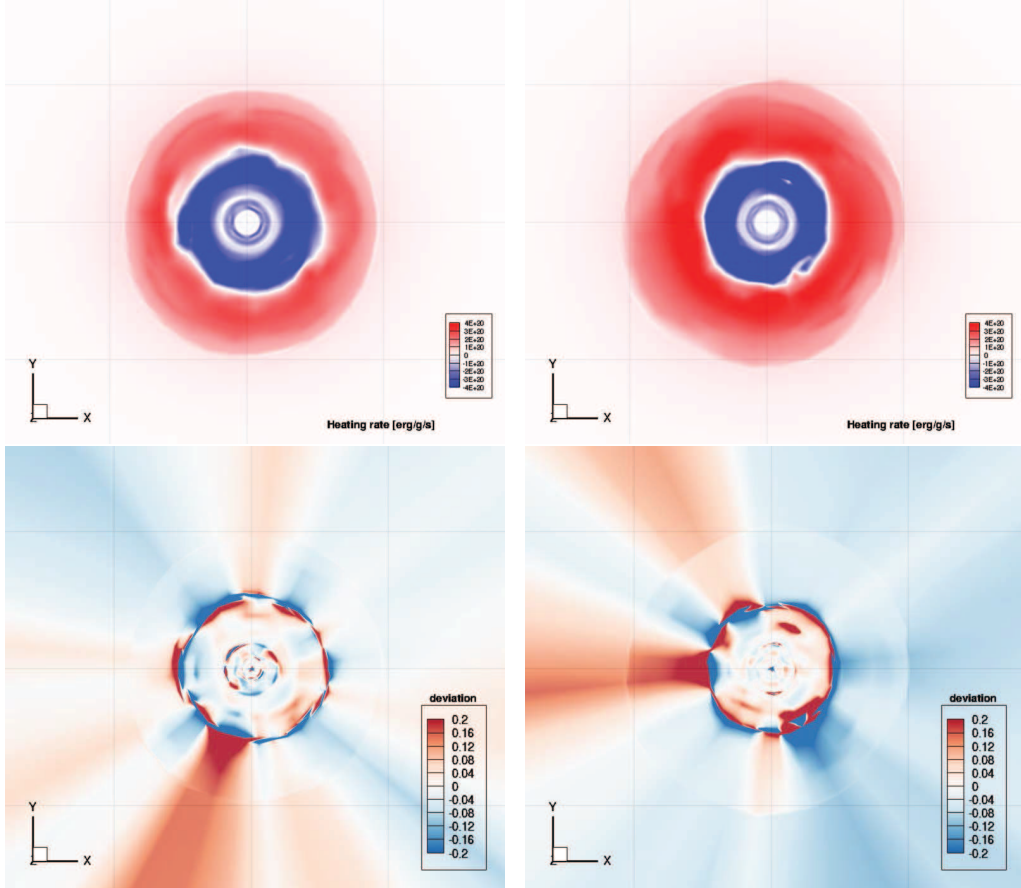


Fig. 30.— Color maps of the heating rate obtained by the 6D Boltzmann solver for the 27M model are shown in the upper panels. The relative difference of the ray-by-ray evaluation is shown in the lower panels. The left and right panels correspond to the snapshots at 150 and 200 ms after the bounce, respectively. Grid lines with 200 km spacing are shown in the background.

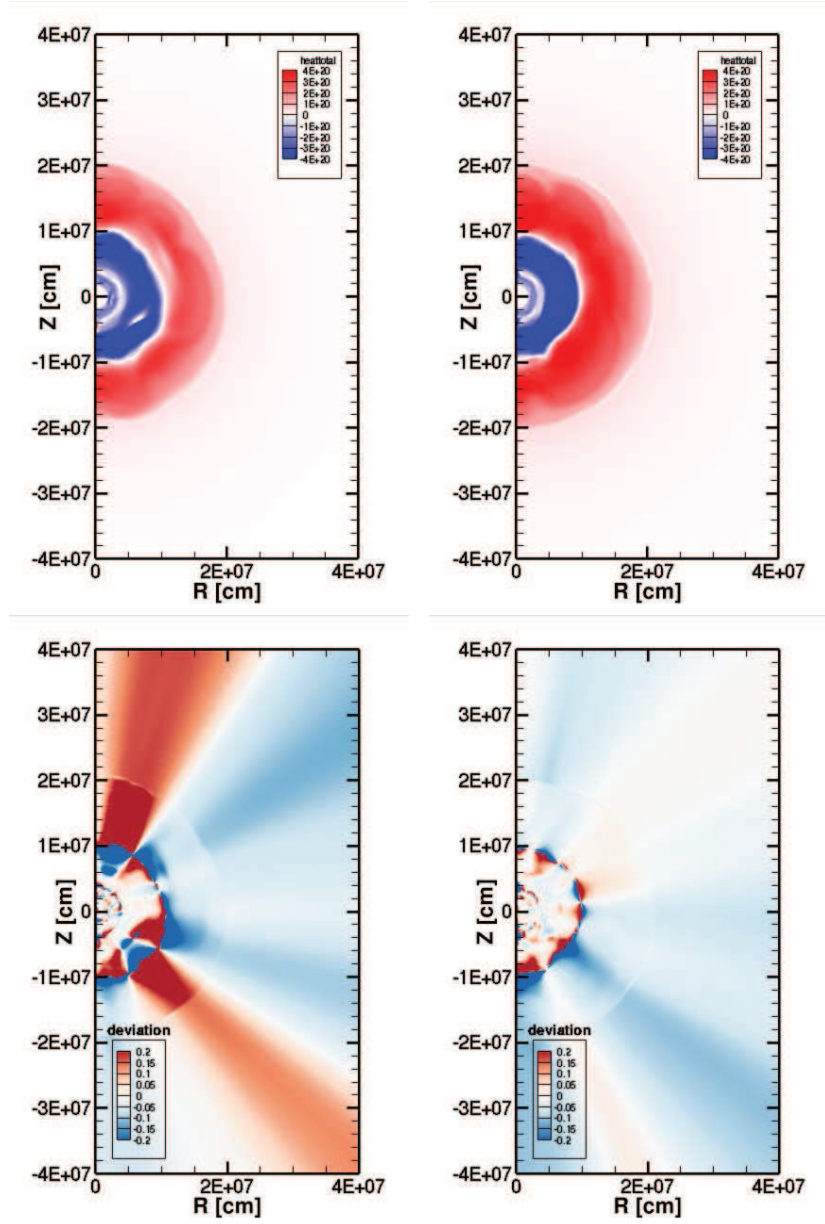


Fig. 31.— Color maps of the heating rate by the 6D Boltzmann evaluation for the 27M model on the meridian slice at  $\phi=51^\circ$  are shown in the upper panels. The corresponding profiles for the relative difference of the ray-by-ray evaluation are shown in the lower panels. The left and right panels correspond to the snapshots at 150 and 200 ms after the bounce, respectively.

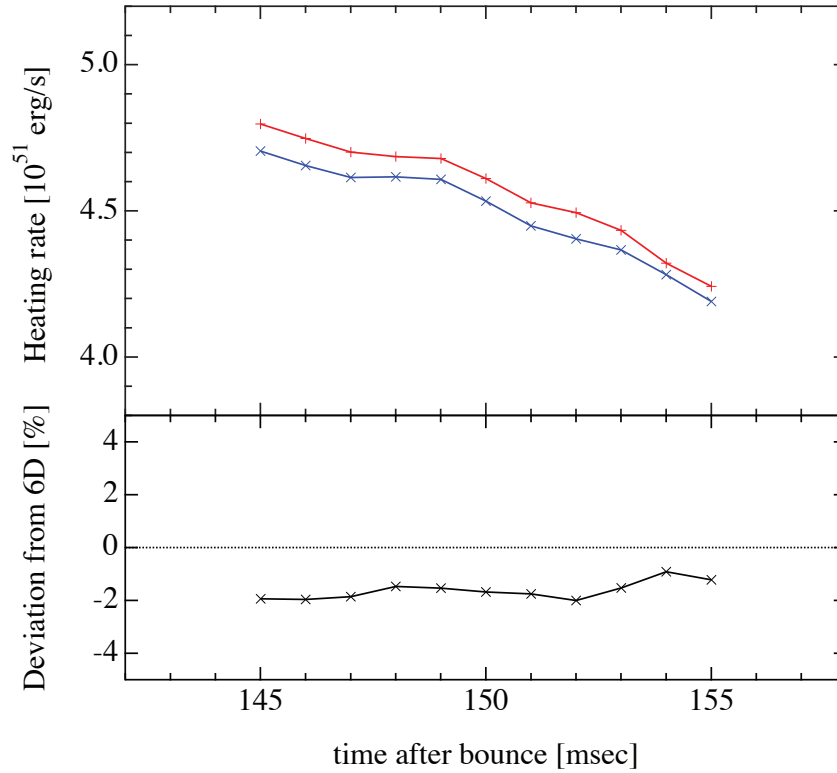


Fig. 32.— The volume-integrated heating rates are shown for the series of snapshots during the time period of 145–155 ms from the 3D supernova simulation (11M). The values at every 1 ms obtained by the 6D Boltzmann and ray-by-ray evaluations are shown by red and blue lines, respectively, with symbols in the upper panel. The relative difference of the ray-by-ray evaluation with respect to the 6D Boltzmann evaluation is shown in the lower panel.

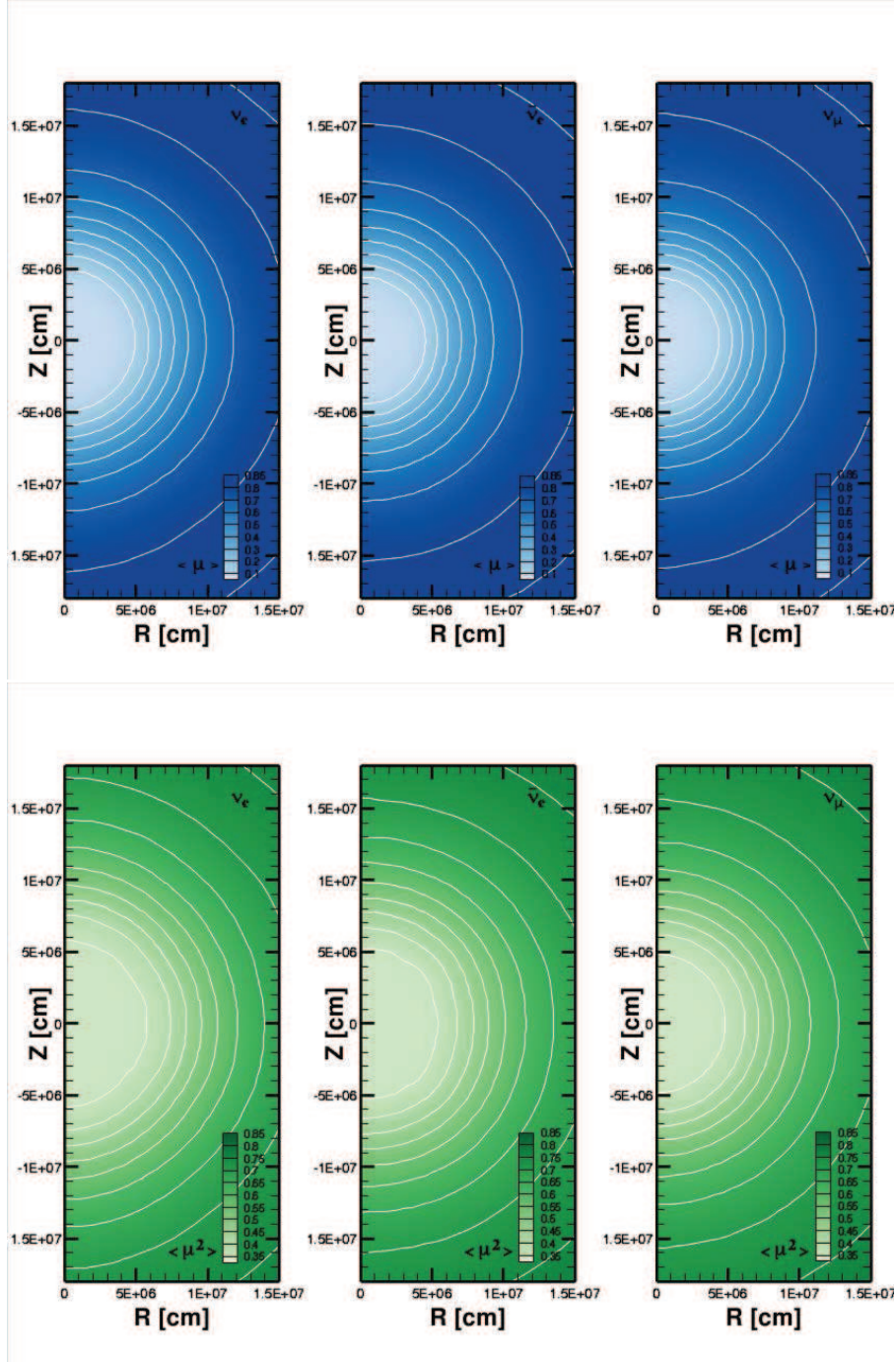


Fig. 33.— Contour maps of the flux factor,  $\langle \mu_\nu \rangle$ , (top) and the second angle moment,  $\langle \mu_\nu^2 \rangle$ , (bottom) on the meridian slice at  $\phi=51^\circ$  are shown for the 11M model at 150 ms after the bounce. The left, middle and right panels display profiles for three species ( $\nu_e$ ,  $\bar{\nu}_e$  and  $\nu_\mu$ ), respectively.

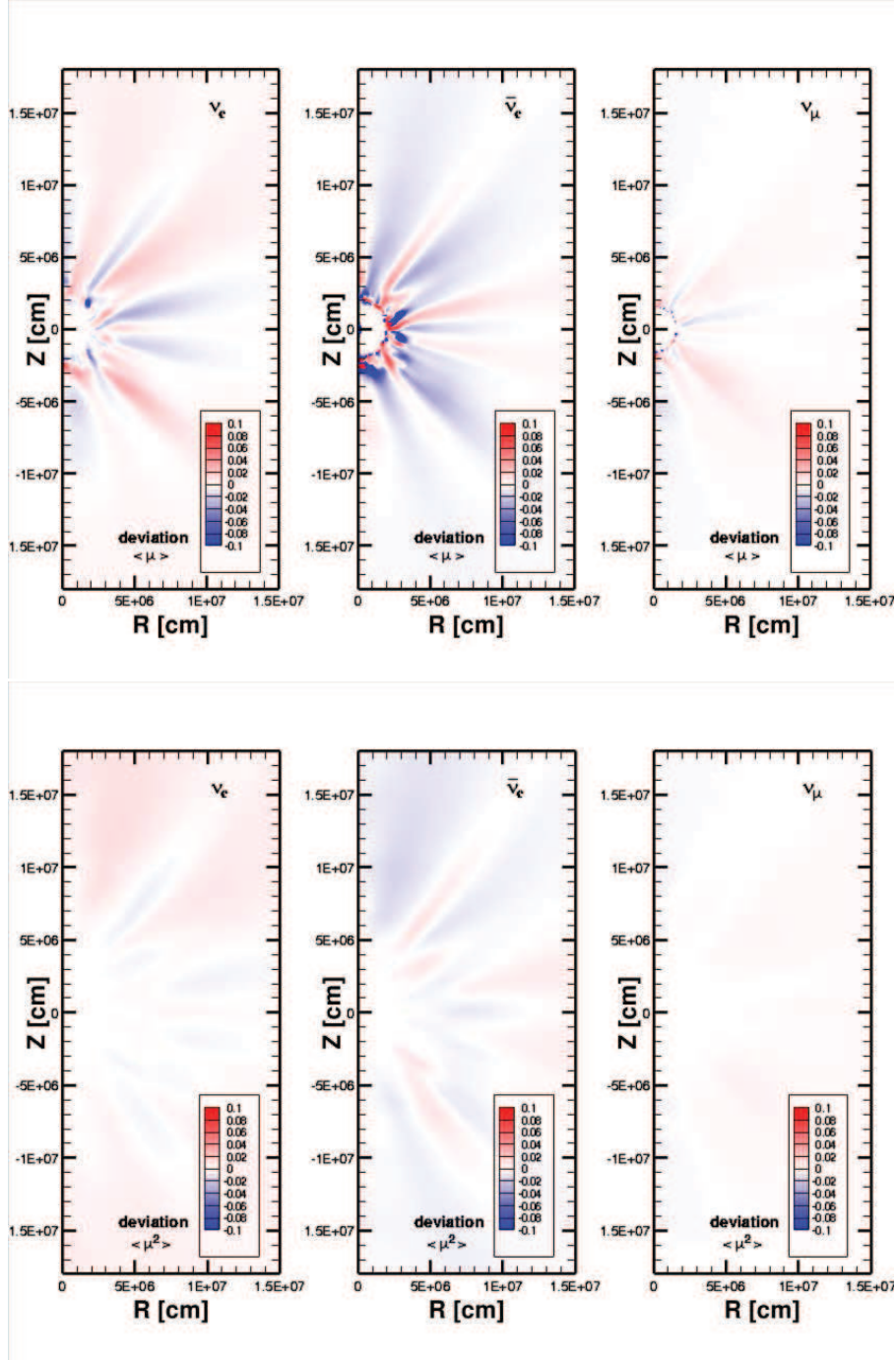


Fig. 34.— Color maps of the relative differences of the ray-by-ray evaluation with respect to the 6D Boltzmann evaluation are shown for the angle moments  $\langle \mu_\nu \rangle$  (top) and  $\langle \mu_\nu^2 \rangle$  (bottom). The left, middle and right panels display profiles for three species ( $\nu_e$ ,  $\bar{\nu}_e$  and  $\nu_\mu$ ), respectively, corresponding to those in Fig. 33.

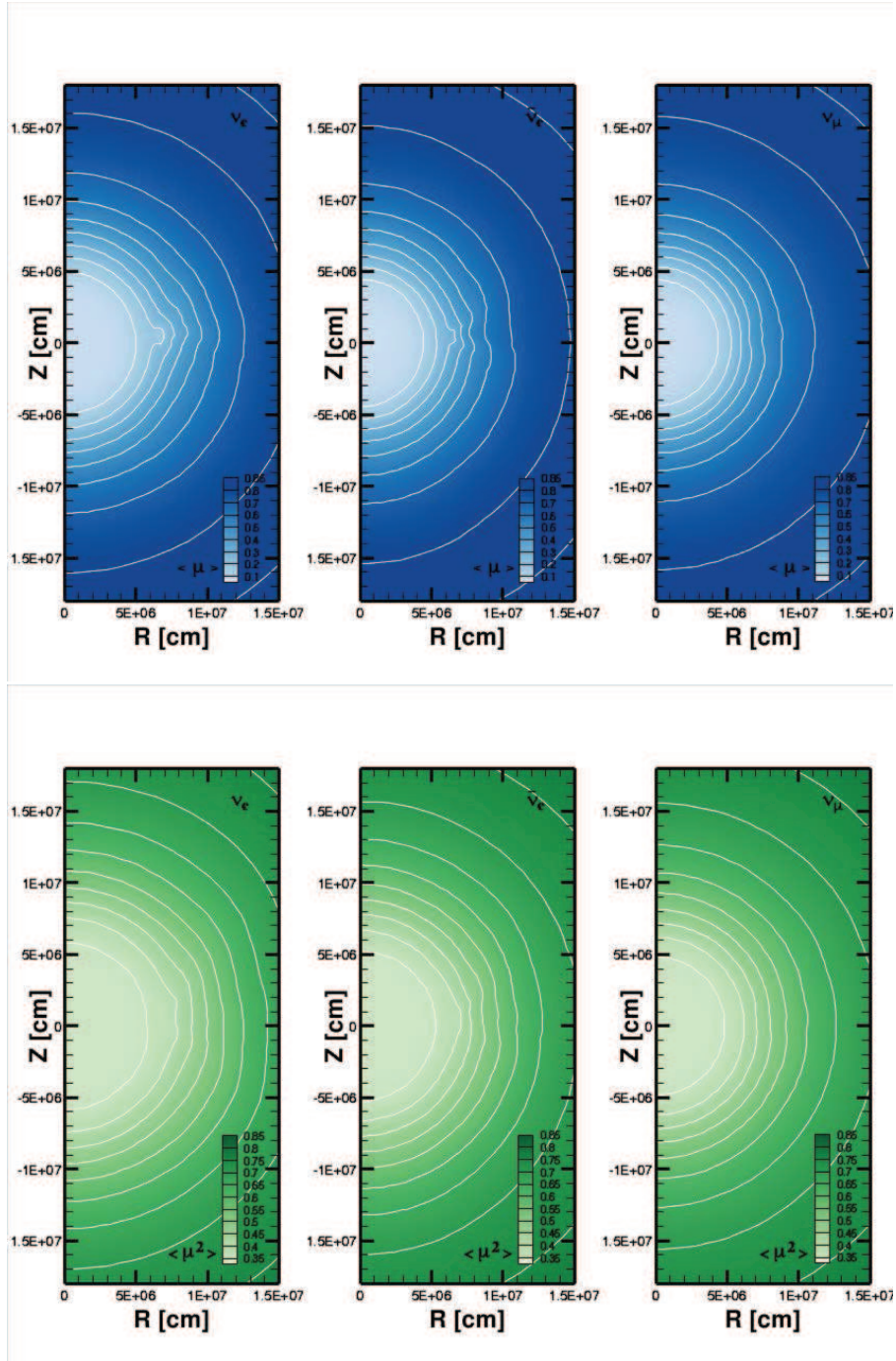


Fig. 35.— Same as Figure 33 but on the meridian slice at  $\phi=141^\circ$ .

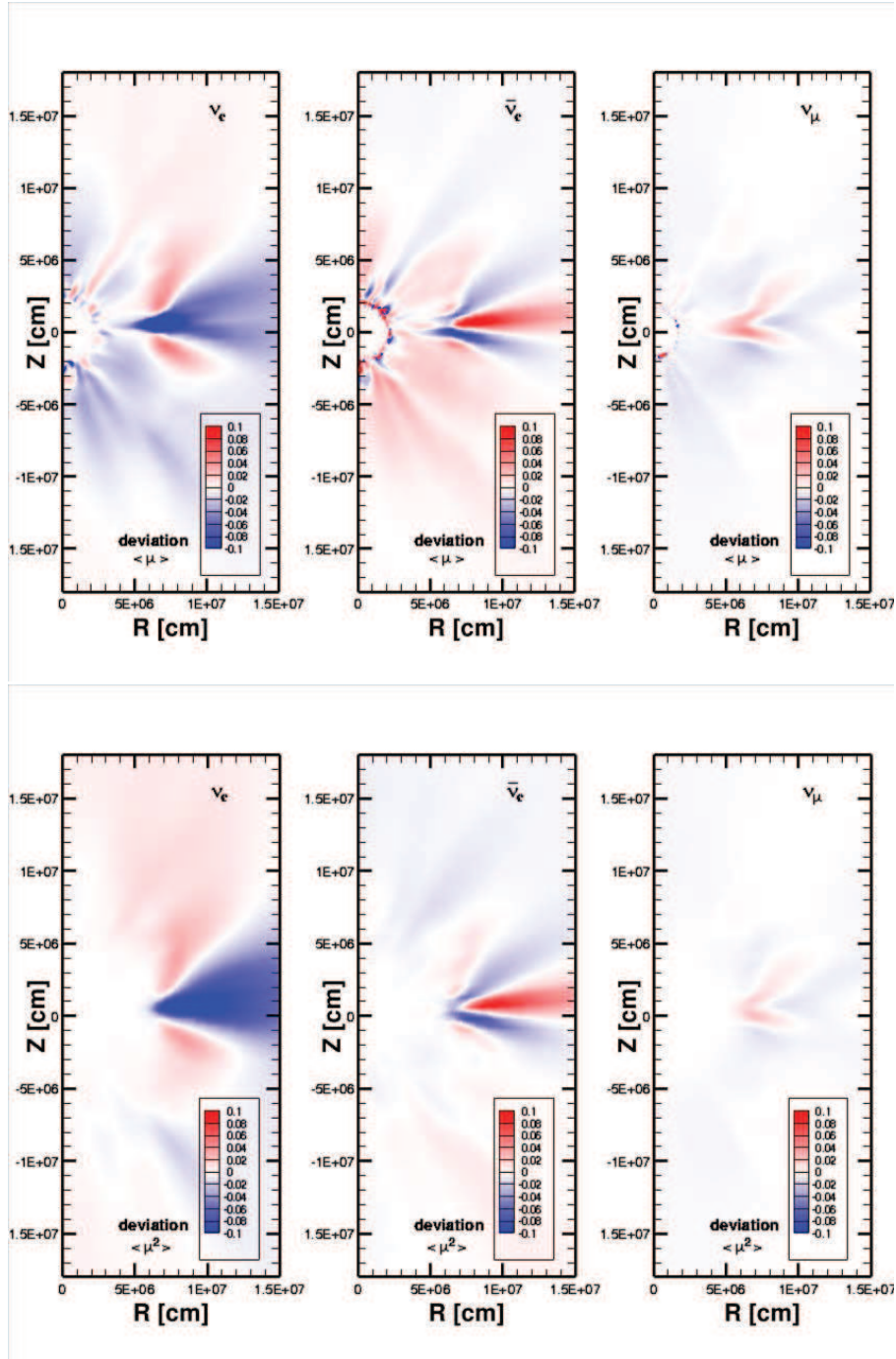


Fig. 36.— Same as Figure 34 but on the meridional slice at  $\phi=141^\circ$ , corresponding to those in Fig. 35.

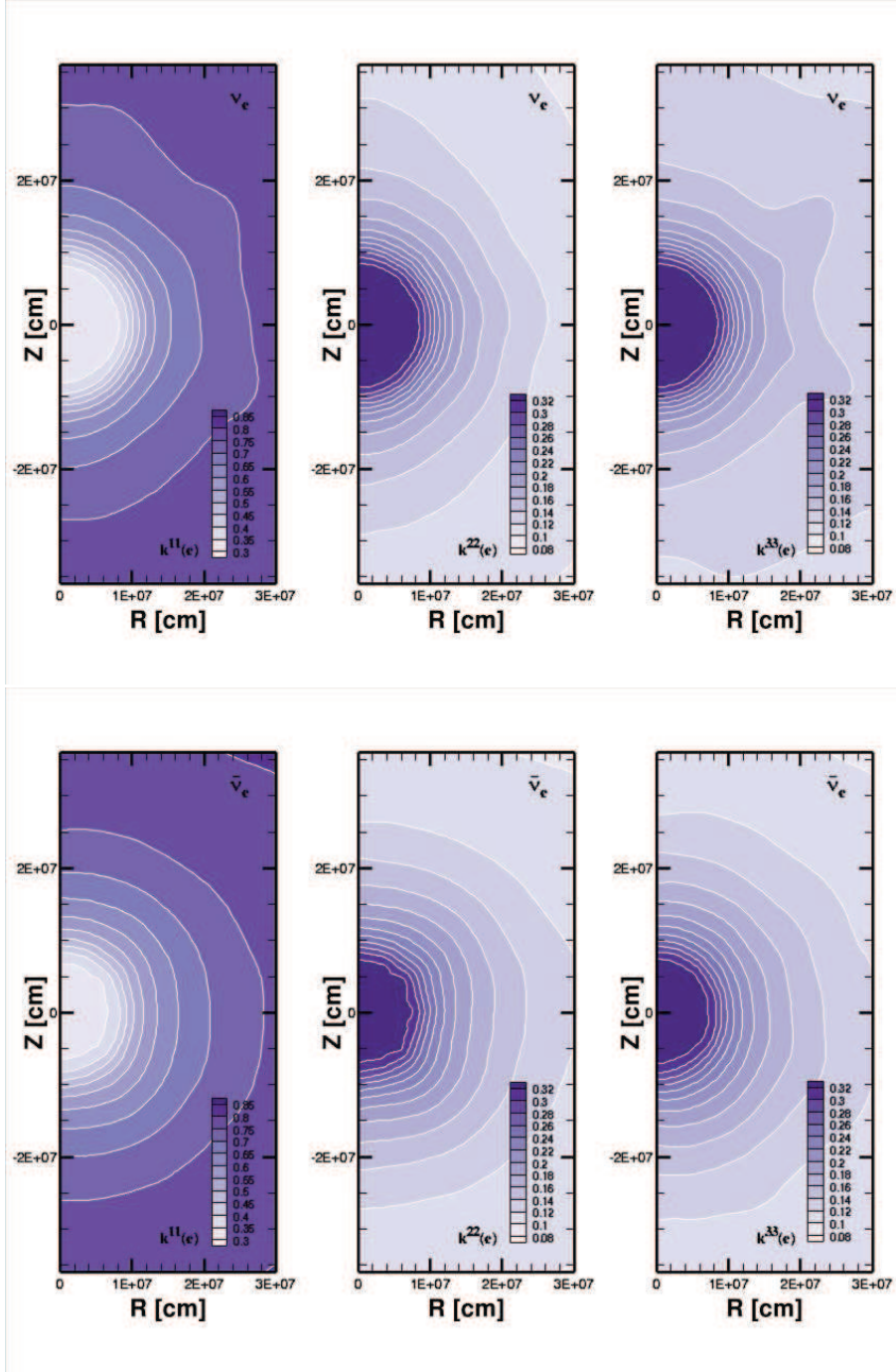


Fig. 37.— Contour maps of the Eddington tensor on the meridian slice at  $\phi=51^\circ$  are shown for the 11M model at 150 ms after the bounce. The diagonal elements for the energy bin ( $E_\nu = 34$  MeV) are shown in the left ( $rr$ ), middle ( $\theta\theta$ ) and right ( $\phi\phi$ ) panels. The profiles for two species  $\nu_e$  and  $\bar{\nu}_e$  are displayed in the top and bottom panels, respectively.

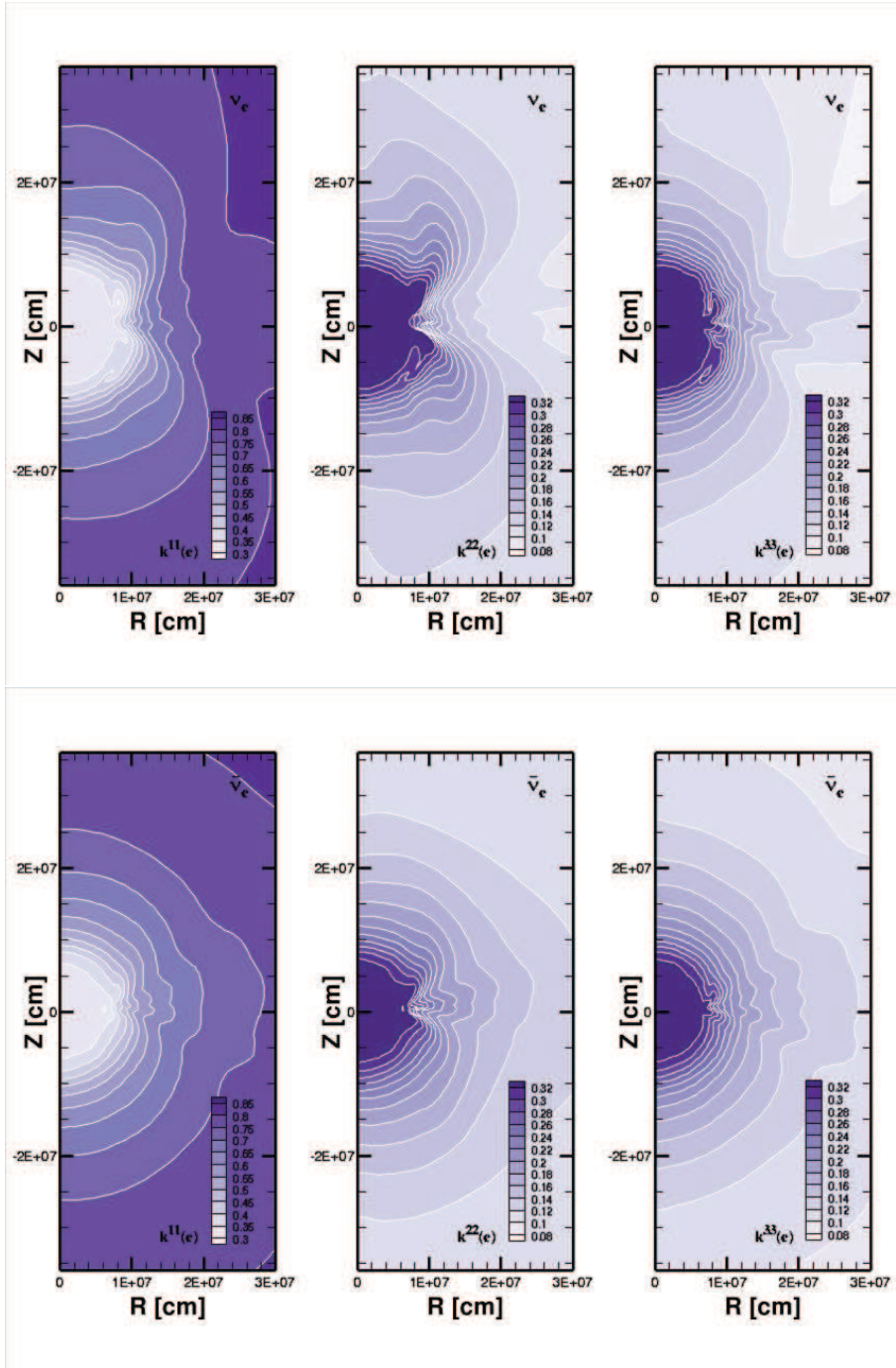


Fig. 38.— Same as Figure 37 but on the meridian slice at  $\phi=141^\circ$ .

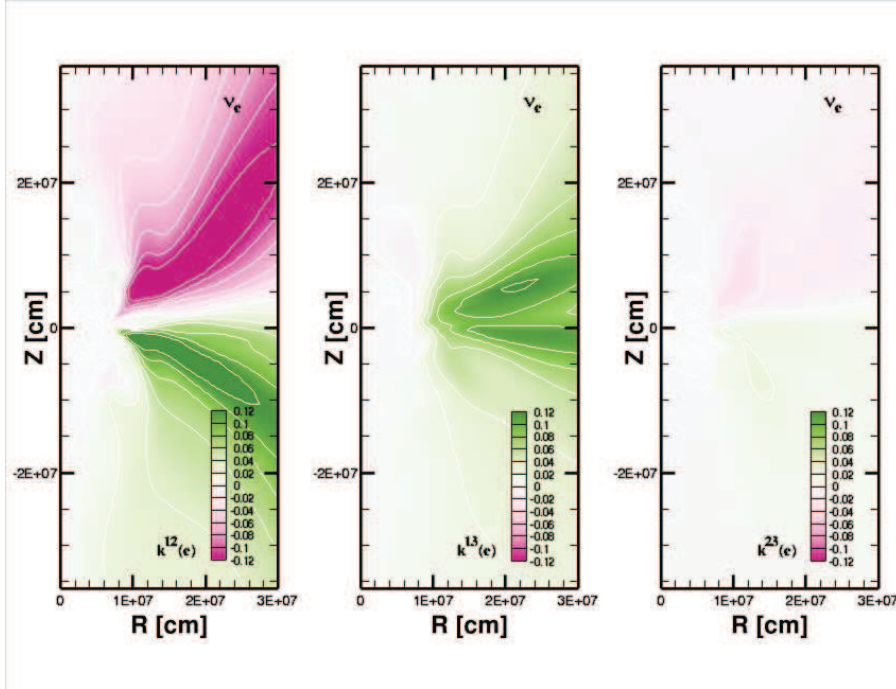


Fig. 39.— Contour maps of the Eddington tensor on the meridian slice of  $\phi=141^\circ$  are shown for the 11M model at 150 ms after the bounce. The non-diagonal elements for the energy bin ( $E_\nu = 34$  MeV) for  $\nu_e$  are shown in the left ( $r\theta$ ), middle ( $r\phi$ ) and right ( $\theta\phi$ ) panels.